Journal of *Marine Science and Engineering*

MDPI

Article

Monitoring and Assessment of Coastal Hazard Potential Induced by Reclamation-Related Subsidence: An Integrated InSAR and Coastline-Change Approach in Fangchenggang, China

Yafei Sun [1,2,*], Kaijie Yang [1], Miaomiao Zhang [2], Mingsheng Zhang [1] and Juanjuan Tang [3]

[1] School of Spatiotemporal Information Engineering, Henan University of Urban Construction, Pingdingshan 467041, China; kaijiey60@gmail.com (K.Y.); 2025105004@huuc.edu.cn (M.Z.)
[2] State Key Laboratory of Precision Geodesy, Innovation Academy for Precision Measurement Science and Technology, Chinese Academy of Sciences, Wuhan 430077, China; zhangmm@apm.ac.cn
[3] Fangchenggang Surveying and Mapping Institute of Housing and Urban-Rural Development, Fangchenggang 538001, China; rise031116@gmail.com
* Correspondence: sunyafei11@mail.ucas.ac.cn

Abstract

Land subsidence in coastal reclamation areas has emerged as one of the critical hidden hazards for coastal cities. This paper presents an integrated InSAR and coastline-change framework for land subsidence monitoring and driving-factor analysis in coastal reclamation cities. Taking the Fangchenggang City, China, as the study area, we utilized 266 scenes of Sentinel-1A SAR images (2016–2025) from the European Space Agency (ESA) and applied time-series SBAS-InSAR to obtain a 10-year time-series monitoring result of land subsidence, with cross-validation against PS-InSAR showing an RMSE below 4 mm at four checkpoints. Furthermore, influencing factors were analyzed by integrating data on coastline changes, precipitation, and groundwater indicators. The conclusions of this paper are as follows: (1) Seven distinct land subsidence funnels in Fangchenggang City from 2016 to 2025 were identified for the first time. Spatially, land subsidence exhibits significant heterogeneity, primarily concentrated in the coastal reclamation areas of the Qisha Peninsula and the Yuwan Peninsula, the maximum subsidence rate reached as high as -163.53 ± 4.90 mm/yr. Temporally, the subsidence rate in the study area shows a gradual deceleration trend over time. (2) The coastline change results from 1964 to 2025 reveal a three-stage temporal characteristic: the land area increased by 2.23 ± 4.51 km^2, 14.28 ± 6.19 km^2, and 23.31 ± 4.51 km^2 during the periods of 1964–1995, 1995–2008, and 2008–2025, respectively. The time-series InSAR results and coastline change results demonstrate that coastal reclamation is the primary factor contributing to land subsidence in this study area. (3) Apart from land reclamation, driving factors such as precipitation and groundwater indicators also show a slight correlation with land subsidence.

Keywords: coastal hazard potential; reclamation; land subsidence; Fangchenggang City; coastline-change; SBAS-InSAR; Sentinel-1; Beibu Gulf

Check for updates

Academic Editor: Deniz Velioglu Sogut

Received: 25 July 2026
Revised: 15 August 2026
Accepted: 18 August 2026
Published: 20 August 2026

Copyright: © 2026 by the authors. Licensee MDPI, Basel, Switzerland. This article is an open access article distributed under the terms and conditions of the Creative Commons Attribution (CC BY) license.

1. Introduction

Land subsidence in coastal reclamation areas has emerged as one of the critical hidden hazards for coastal cities [1,2]. Following the implementation of reclamation projects, most coastal cities experience instability phenomena such as land subsidence, which jeopardizes the safety of urban infrastructure, including buildings, roads, and railways [3]. As a typical

coastal reclamation city, Fangchenggang has undergone large-scale reclamation projects in recent decades [4]. Such massive reclamation inevitably poses a serious threat to the city's stability, making it urgent to clarify the underlying factors contributing to land subsidence. Currently, the absence of large-scale, high-resolution, and high-precision monitoring data means that the spatial patterns, temporal trends, and hazard potential of land subsidence in the study area remain largely unknown.

Coastal cities are frequently subjected to various hazards, such as tsunamis, coastal flooding, and sea-level rise. Remote sensing-based monitoring and assessment of tsunamis, exposure assessment of coastal flooding, and prediction of sea-level rise hazards have received considerable attention and investigation from numerous scholars [5–9], yielding a wealth of important findings that have provided critical data support and decision-making foundations for hazard management and prevention in relevant cities. However, land subsidence in reclaimed areas of coastal cities—a potential hazard that may pose a significant threat to the normal operation and stability of urban areas—has received relatively less attention and research in terms of monitoring and analysis of this latent hazard.

Current land subsidence monitoring methods can be broadly categorized into two branches: traditional surveying and satellite remote sensing technologies [10]. While traditional approaches, such as precise leveling and continuous GNSS (Global Navigation Satellite System) observation stations, offer the advantage of high single-point accuracy, they suffer from significant limitations-including sparse monitoring network density, high labor maintenance costs, and insufficient spatiotemporal continuity [11]. Consequently, they struggle to meet the demands for large-scale dynamic monitoring in modern cities. In contrast, Interferometric Synthetic Aperture Radar (InSAR) technology overcomes the constraints of traditional techniques through multi-temporal interferometric processing algorithms (e.g., PS-InSAR, SBAS-InSAR), enabling large-scale, high-spatial-resolution, and continuous time-series land subsidence monitoring [12–14]. In particular, the open data policy of the Sentinel-1 satellite constellation provides time-series InSAR with a significant cost advantage. Its millimeter-level land subsidence monitoring accuracy has been validated across numerous cities, establishing it as an indispensable technical tool in the field of urban land subsidence monitoring [15–19].

As a global environmental geological issue, urban land subsidence has evolved into a significant hidden hazard threatening urban safety since it was first discovered in Mexico City in the late 19th century. In 2024, Ao et al. utilized time-series InSAR to systematically assess land subsidence across China's major cities (2015–2022) [15]. Their study revealed that 45% of urban lands were subsiding faster than 3 mm/yr, significantly threatening sustainable development. Results indicated that excessive groundwater withdrawal and heavy infrastructure were primary drivers, and projected that 22–26% of coastal lands would fall below sea level by 2120 due to the combined impact of subsidence and sea-level rise. Currently, monitoring land subsidence in coastal reclamation cities is receiving increasing attention from researchers. In 2010, Jiang et al. utilized time-series InSAR to investigate the long-term reclamation subsidence at Hong Kong's Chek Lap Kok Airport [2]. The analysis revealed that the original islands and pile-founded structures remained stable, whereas the reclaimed areas exhibited moderate (3–7 mm/yr) to severe (>10 mm/yr) subsidence. The study attributed this differential subsidence to variations in fill thickness and alluvial soil properties, with ongoing primary consolidation driving the high subsidence rates observed up to 2008. In 2018, Sun et al. developed an improved distributed scatterer InSAR strategy to monitor subsidence at Hong Kong's reclaimed areas [1]. Applied to Hong Kong International Airport, this method drastically reduced computational time while detecting significantly more measurement points than traditionally PS-InSAR techniques. The results revealed detailed differential subsidence patterns, with the InSAR-derived deformation

rates showing high consistency with leveling survey measurements, thereby validating the effectiveness of the proposed approach. In 2022, a study on Xiamen and Zhangzhou utilized 125 Sentinel-1A images and InSAR techniques (SBAS and DS-InSAR) to monitor land subsidence [16]. Results showed severe cumulative deformation, reaching 626 mm on Shuangyu Island. By applying sequential estimation and geotechnical models, the research predicted a maximum deformation of 1.1 m by 2026, providing critical data for infrastructure safety in coastal reclamation areas. In 2024, Wang et al. utilized a large stack of Sentinel-1A imagery to investigate the deformation characteristics of the Funing Bay reclamation embankment in China [17]. By optimizing the phase-unwrapping process, the study revealed that the maximum subsidence rate exceeded 50 mm/yr, with internal embankment areas showing higher deformation levels than those closer to the sea. Time-series analysis indicated a gradual deceleration in the deformation rate, providing insights for the safe operation of coastal reclamation projects. In 2025, Jiang et al. utilized time-series InSAR to investigate the Hong Kong International Airport's third runway, where Deep Cement Mixing (DCM) was employed for reclamation [18]. Results showed a maximum subsidence rate of approximately 150 mm/yr. The study revealed that DCM achieves stability faster than Prefabricated Vertical Drains (PVD), effectively controlling primary settlement to 29–83% of the PVD method, and offers a time advantage of 0.08–1.39 years. In 2026, Zhang et al. utilized time-series InSAR to investigate land subsidence in lake-reclaimed urban areas of Wuhan [19]. The study revealed that subsidence rates are stage-dependent, influenced by the consolidation of soft soils and infilling periods. Results showed cumulative subsidence reaching 31.05 mm in Shahu Lake, with engineering activities and irrigation further intensifying deformation, clarifying the mechanisms of subsidence in infilled landscapes.

Beyond land subsidence monitoring studies conducted within China, significant research achievements have also been made by scholars worldwide in regions such as Jakarta, Semarang, Venice, the Netherlands, South Korea, the Philippines, and other countries and territories [20–27]. In 2011, Abidin et al. employed multi-source observation methods including leveling, GNSS, and InSAR to reveal significant spatial differences in land subsidence in Jakarta and its relationship with urbanization development, indicating that local subsidence could reach centimeters per year [20]. In 2018, Tosi et al. utilized TerraSAR-X Permanent Scatterer Interferometry (PSInSAR) techniques to conduct high-density deformation monitoring in the Venetian coastal zone, obtaining fine-scale spatial distribution characteristics under the combined effects of natural subsidence and anthropogenic activities, and enhancing the capability to identify subsidence mechanisms along the Venice coast [22]. Notably, in 2023, Park et al. monitored subsidence in reclaimed areas along the west coast of South Korea using Sentinel-1 imagery and PSInSAR technology [24]. The results showed that the proportion of high-confidence subsidence points in reclaimed areas was seven times that of natural ground surfaces. Key findings indicated that the "interval between filling and construction" governs long-term stability: areas with short intervals required 11 years for subsidence to stabilize, whereas areas with long intervals required only 6 years [24]. This study revealed that reclamation subsidence is regulated by the timing of development, providing insights for the present research. In 2023, Lomibao et al. utilized Sentinel-1 imagery from 2018 to 2021 and PS-InSAR technology to monitor deformation across four reclamation islands in the Manila Bay Freeport Zone [25]. The results showed that the reclaimed areas were generally stable but exhibited localized subsidence, with the CBP-IB&IC island experiencing an average subsidence rate of −2.53 mm/yr and a maximum rate of −17.60 mm/yr [25]. This study confirmed that PS-InSAR can effectively identify localized deformation in reclaimed areas, likewise offering ideas for the research presented in this paper. These prior time-series InSAR studies on subsidence monitoring in

coastal reclamation cities provide a crucial foundation and valuable insights for the stability monitoring and analysis conducted in this work.

It should be noted that the land subsidence results derived from time-series InSAR contain errors such as unwrapping errors, DEM errors, and atmospheric errors, and it is imperative to perform unwrapping-error detection, DEM-error estimation, and validation of atmospheric corrections [28–31]. In 2013, Fattahi et al. developed estimation and correction approaches for residual DEM errors in time-series InSAR, revealing that DEM errors can influence deformation time series via the perpendicular baseline history, and that temporal correction can enhance deformation retrieval [28]. In 2021, Xiao et al. proposed a statistical evaluation framework for GACOS atmospheric correction, incorporating phase standard deviation, spatial structure function, and phase-elevation correlation coefficient as metrics, and found that GACOS reduced phase standard deviation in 84.6% of Sentinel-1 interferograms by an average of 36.4% [29]. In 2022, Ma et al. introduced a phase unwrapping error correction technique combining incoherent phase correction, triangular phase closure tests, and integer linear programming, which effectively improved unwrapping accuracy and mitigated creep model uncertainties induced by unwrapping errors [30]. In 2023, Olsen et al. constructed an uncertainty assessment framework for InSAR-derived deformation using simulated SAR data stacks and ensemble analysis, enabling precision quantification at both pixel and temporal scales [31]. These studies provide valuable insights for the error suppression and uncertainty estimation of InSAR in this paper.

In recent years, stability monitoring and analysis in Fangchenggang City have garnered increasing attention. In 2024, Luo et al. utilized time-series InSAR to obtain land subsidence results for the coastal areas of the Beibu Gulf in Guangxi from 2018 to 2020, analyzing factors such as precipitation and human activity intensity [32]. However, their results did not reveal significant subsidence funnel signals in the Gangkou District of Fangchenggang City. Also in 2024, Ming et al. employed SBAS-InSAR to acquire land subsidence results for the Qinzhou-Fangchenggang region from 2018 to 2021, analyzing major subsidence factors including urban expansion, road density, tectonic movement, precipitation, and sea-level rise, yet they did not analyze the critical factor of land reclamation [33]. In 2024 and 2026, Ming et al. and Gao et al. respectively utilized time-series InSAR to monitor land subsidence in the Maowei Sea tidal flats, concluding that precipitation, hydrological dynamics, sea-level rise, and mangrove changes were the dominant factors [34,35]. While the aforementioned literature provides valuable insights for researching land subsidence and influencing factors analysis in Fangchenggang City, none have elaborated in detail on the impact of land reclamation—a crucial factor—on the city's subsidence. The possible reason for this gap is likely that the time-series InSAR results were not sufficiently refined to identify distinct subsidence funnel signals, thereby precluding a detailed analysis of the impact of land reclamation on land subsidence.

Therefore, to address the above issues, this paper takes the Fangchenggang City as the study area, utilizes 266 scenes of Sentinel-1A data from the European Space Agency (ESA), and employs time-series InSAR to obtain land subsidence results for the study area from 2016 to 2025. Combined with coastline-change results from 1964 to 2025, as well as precipitation and groundwater, and the driving factors of the study area are analyzed to provide data support and a decision-making basis for the rapid development and stable urban operation of Fangchenggang City.

2. Materials and Methods

2.1. Study Area

Fangchenggang City (21°29′~22°22′ N, 107°28′~108°36′ E) is located in the southern border area of Guangxi, as shown in Figure 1. The southern sea area of this city is the

Beibu Gulf, and it borders Vietnam in the southwest. It is a coastal and border city with an area of approximately 6176 km^2 [36]. It governs four counties (districts and cities), namely the Gangkou District, Fangcheng District, Dongxing City, and Shangsi County [36]. The climate in this region is characterized as a monsoon climate in southeastern Asia, featuring hot and humid conditions with abundant rainfall. The multi-year average annual precipitation is approximately 2000 mm, with rainfall mainly concentrated from June to November [33]. The shallow marine sediments along the coast of this region are dominated by silt and clay, and due to sedimentation, a thick layer of soft soil exists along the coast of Fangchenggang [37]. In addition, as an important coastal city in Guangxi, Fangchenggang also faces threats from various marine disasters such as storm surges, sea-level rise, and coastal erosion.

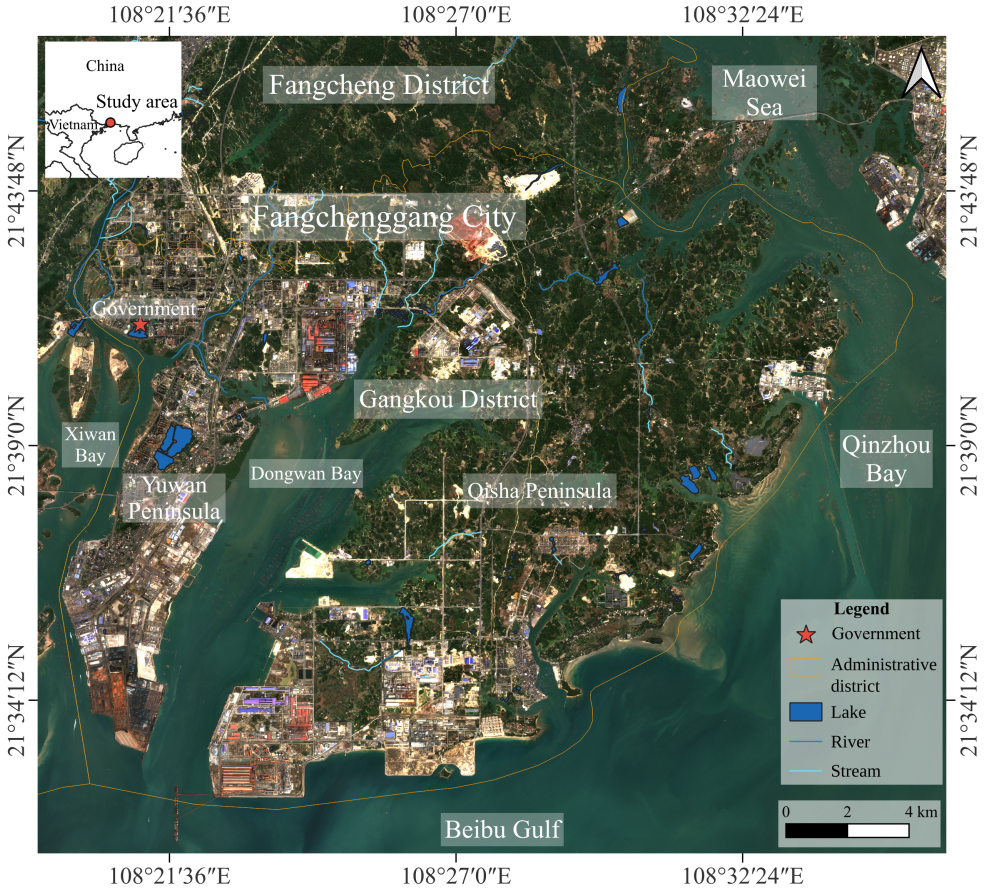


Figure 1. The spatial location of the study area.

Fangchenggang City has a coastline of 552.93 km, of which 204.69 km is natural coastline and 348.24 km is artificial coastline, with artificial coastline accounting for as much as 62.98%. Since the 1980s, large-scale land reclamation projects have been continuously carried out on the Qisha Peninsula and the Yuwan Peninsula in the study area, primarily for purposes such as port construction, urban development, and mariculture [4,38]. Since the reclamation projects in Fangchenggang City are mainly concentrated in the Gangkou District, this study takes the Gangkou District of Fangchenggang City as the study area for stability monitoring and analysis. Benefiting from these reclamation projects, Fangchenggang has become the largest port in western China and a key international gateway port under the nationally supported New International Land-Sea Trade Corridor in the western region, with its cargo throughput consistently ranking among the top in the country.

2.2. Data Source

2.2.1. Sentinel-1 SAR Data

Sentinel-1A, launched in 2014, remains in orbit and operational to this day. Sentinel-1B, launched in 2016, was retired in 2021 due to a power supply failure and has since been succeeded by Sentinel-1C, launched in 2024, and Sentinel-1D, launched in 2025. The Sentinel-1 satellites are placed in a sun-synchronous orbit and carry a C-band synthetic aperture radar (SAR) sensor, with an orbital altitude of 693 km. Sentinel-1 has four imaging modes: StripMap (SM), Interferometric Wide swath (IW), Extra-Wide swath (EW), and Wave Mode (WV) [39]. The Interferometric Wide swath (IW) mode is commonly used for urban land subsidence monitoring, with azimuth and range resolutions of 20 m and 5 m, respectively [39]. The experimental data used in this study are Sentinel-1A SAR images acquired from 20 January 2016 to 29 December 2025, totaling 266 scenes. The imaging mode is Interferometric Wide-swath (IW), the orbit type is ascending, the polarization is VV, and the data product level is Single Look Complex (SLC) SAR images.

2.2.2. Optical Remote Sensing Data

This study also acquired declassified US military reconnaissance satellite imagery from the KeyHole (KH) program [40], along with long time-series optical remote sensing images such as Landsat 8, Google Earth historical imagery, and Sentinel-2A, to extract historical coastline changes and analyze the spatio-temporal evolution characteristics of land reclamation activities. Landsat 8, Google Earth historical imagery, and Sentinel-2A have been described in detail in multiple published references and will not be further elaborated in this paper [41–43]. It is worth noting that the KH satellite (CORONA), launched between 1960 and 1972, can achieve meter-level spatial resolution [44], which is highly valuable for studying coastline changes between 1960s and 1980s. This study selected KH satellite images from 1964 and 1975 for the identification of historical coastlines. By integrating optical remote sensing data from Landsat 8, Google Earth historical imagery, and Sentinel-2A, the coastline changes in the study area from 1964 to 2025 were extracted, providing data support for the analysis of land subsidence caused by reclamation. It should be noted that CORONA imagery exhibits severe geometric distortions [45–47]. To address this issue, we applied geometric registration to reference images using a second-order polynomial transformation. The detailed workflow is as follows: the CORONA images and reference imagery were loaded into ArcGIS software (version 10.7), and 10–20 ground control points (such as road intersections and building corners) were selected within the study area. After performing the second-order polynomial registration, the residual RMSE was constrained to within 1.5 pixels. Subsequently, georeferenced CORONA images with geographic coordinates were successfully obtained.

2.2.3. Other Experimental Data

In time-series InSAR data processing, the interferometric phase contains error sources such as topographic errors, orbital errors, and atmospheric errors. This study employed the ASTER GDEM with a spatial resolution of 30 m as an external reference DEM to remove topographic-induced errors in the interferometric phase [48], thereby improving the accuracy and reliability of land subsidence monitoring. POD (Precise Orbit Determination) data were also used to correct orbital errors and reduce the impact of orbital residuals on the accuracy of urban land subsidence monitoring. The high-resolution tropospheric delay correction product GACOS (Generic Atmospheric Correction Online Service for InSAR) atmospheric model was applied to mitigate or remove atmospheric phase delays in the interferometric phase [49]. In addition, to analyze the effects of precipitation, groundwater,

and human activities on land subsidence, this study also utilized meteorological data and hydrological data.

2.3. Research Methods

This study employs two time-series InSAR methods, SBAS-InSAR and PS-InSAR, to extract land subsidence results in the study area over the past decade from 2016 to 2025. Each of the two time-series InSAR methods has its own advantages and disadvantages. SBAS-InSAR does not require very high coherence for its points, resulting in a high point density, making it suitable for land subsidence monitoring in non-urban areas. In contrast, PS-InSAR requires very high coherence for its points, leading to a relatively sparse point distribution, which makes it suitable for land subsidence monitoring in urban areas. Since most of the land subsidence in the study area occurs in reclamation areas, this paper uses SBAS-InSAR to monitor land subsidence in the study area, while the PS-InSAR land subsidence monitoring results are used for cross-validation. It is worth noting that the land subsidence rates derived from SBAS-InSAR and PS-InSAR in this study are both in the LOS (Line of Sight) direction. Additionally, this study employs threshold segmentation and visual interpretation methods to extract the coastline changes from 1964 to 2025. The overall framework of this study is shown in Figure 2.

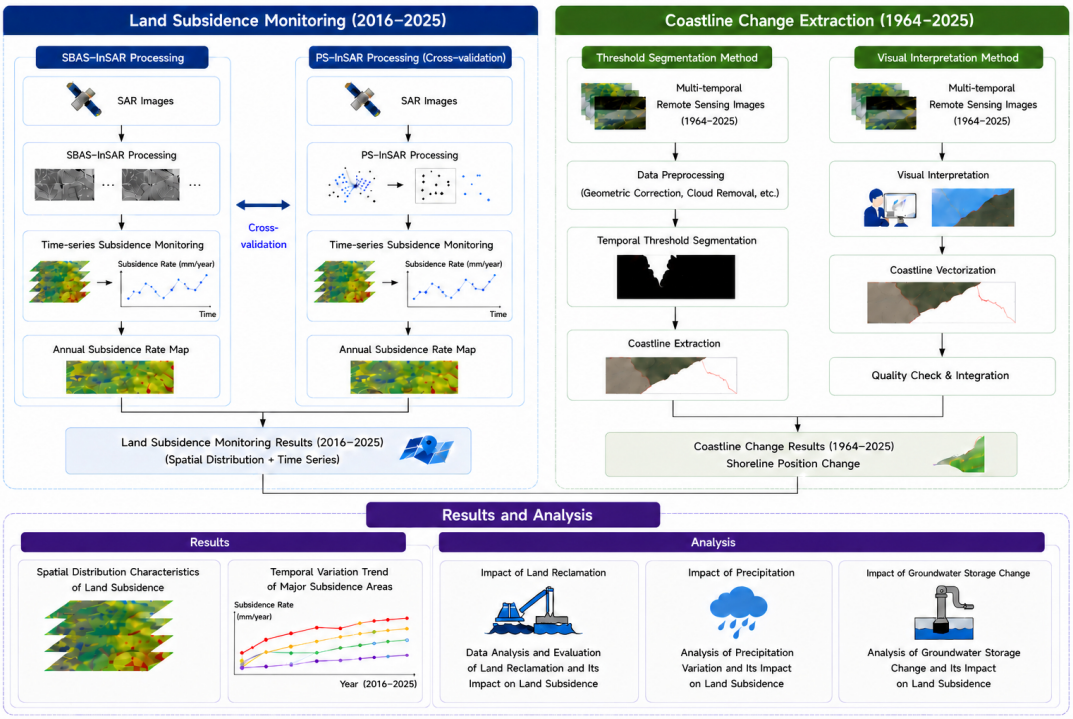


Figure 2. The overall framework of this study.

2.3.1. Time-Series SBAS-InSAR Method

The time-series SBAS-InSAR method, proposed by Berardino et al. [50], is a time-series InSAR approach based on constraints of small temporal baselines and small spatial baselines. By constructing an ensemble of interferometric pairs with small baselines, this method effectively reduces the effects of spatial decorrelation and temporal decorrelation, thereby enhancing the reliability of the interferometric phase and enabling high-precision retrieval of surface deformation.

First, $N + 1$ multi-temporal SAR images covering the study area are acquired. The images are screened based on predefined temporal baseline and spatial baseline thresholds to construct an ensemble of interferometric pairs that meet the specified conditions.

Assuming the final number of interferometric pairs formed is M, the following condition is satisfied:

$$\frac{N+1}{2} \leq M \leq \frac{N(N+1)}{2} \tag{1}$$

For the i-th interferometric pair, the differential interferometric phase generated from the SAR image t_A and the image t_B can be expressed as:

$$\delta\phi_i(x,y) = \phi_B(x,y) - \phi_A(x,y) \approx \delta\phi^i_{disp}(x,y) + \delta\phi^i_{topo}(x,y) + \delta\phi^i_{atm}(x,y) + \delta\phi^i_{noise}(x,y) \tag{2}$$

Here, (x,y) represent the azimuth and range coordinates of the SAR image, respectively; $\delta\phi^i_{disp}(x,y)$ is the deformation phase, $\delta\phi^i_{topo}(x,y)$ is the residual topographic phase, $\delta\phi^i_{atm}(x,y)$ is the atmospheric delay phase, and $\delta\phi^i_{noise}(x,y)$ is the noise phase. If the effects of residual topography, atmospheric delay, and noise are neglected, it can be approximated as:

$$\delta\phi_i(x,y) \approx \frac{4\pi}{\lambda}[d(t_B,x,y) - d(t_A,x,y)] \tag{3}$$

Here, λ is the radar wavelength, and $d(t,x,y)$ represents the cumulative deformation in the line-of-sight (LOS) direction at time t.

After generating the interferometric pairs, we need to inspect both the interferograms and their coherence. Interferometric pairs with poor interferometric quality or low coherence are then discarded before proceeding with subsequent deformation calculations.

Assuming that the average deformation rate for the time period corresponding to the i-th interferometric pair is $v_{k,k+1}$, the cumulative deformation can be expressed as:

$$\delta\phi^i_{disp}(x,y) = \frac{4\pi}{\lambda}\sum_{k=t_A}^{t_B-1} v_{k,k+1}(t_{k+1} - t_k) \tag{4}$$

By combining all interferometric pairs, a matrix equation can be established:

$$Av = \delta\phi \tag{5}$$

Here, A is the matrix, v is the deformation rate vector, and $\delta\phi$ is the observed phase vector. The system of equations can be solved using the least squares method or singular value decomposition (SVD) to obtain the deformation rate for each time interval, and further integration over time yields the cumulative deformation at each observation time. The detailed workflow of the time-series SBAS-InSAR is shown in Figure 3.

The software used in this study is SARscape version 5.6.2, with a temporal baseline of 180 days. The number of looks in the range and azimuth directions is set to 4 and 1, respectively. Phase unwrapping was performed using the Delaunay MCF method. The specific parameters are detailed in Table 1.

Table 1. Parameters for time-series InSAR data processing in this study.

Parameter Name	Parameter Value
Software name	SARscape
Software version	5.6.2
Temporal baseline	180 days
Spatial baseline threshold	200 m
Max Normal Baseline	2%
Range looks	4
Azimuth looks	1
Coherence threshold	0.25
Phase unwrapping algorithm	Delaunay MCF

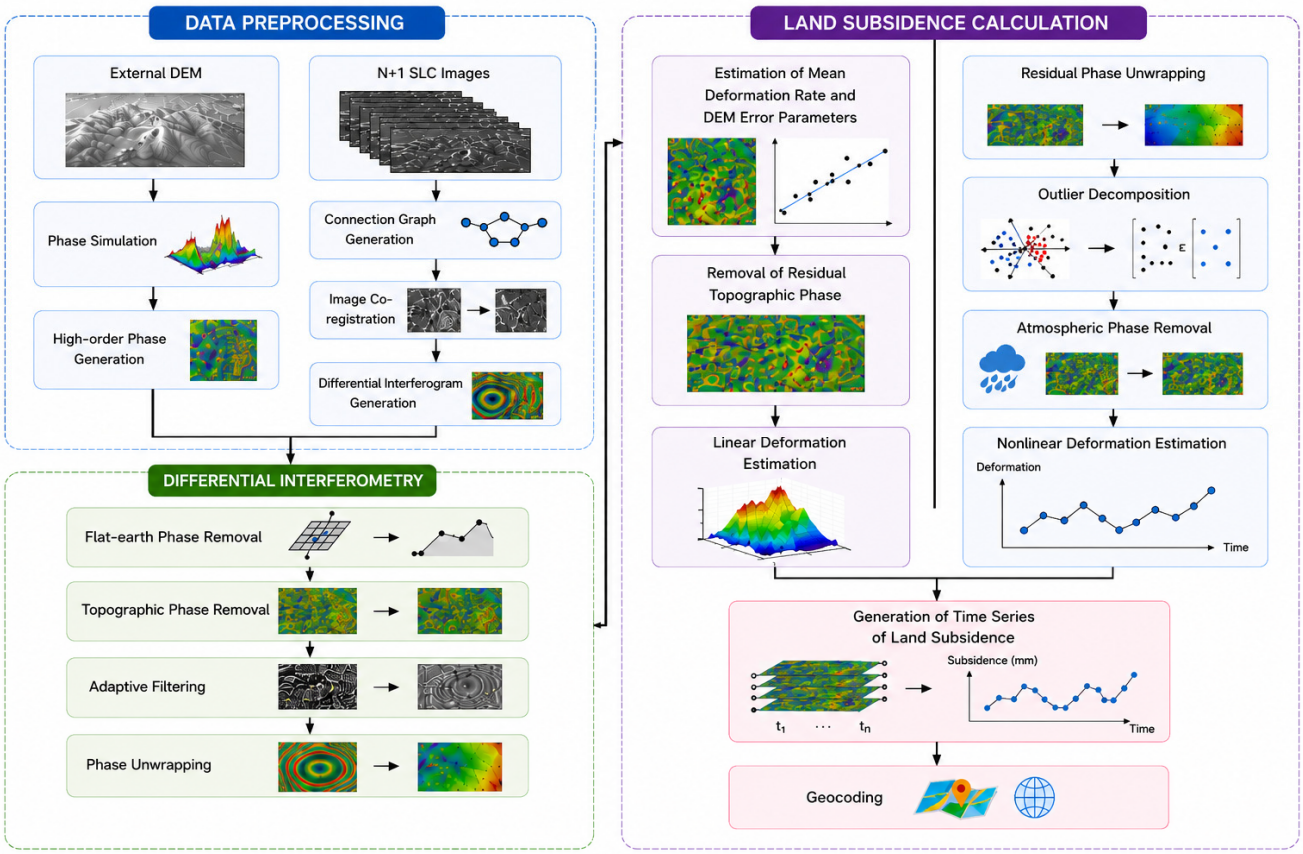


Figure 3. The flowchart of the time series SBAS-InSAR method.

2.3.2. Time-Series PS-InSAR Method

The PS-InSAR method is a time-series InSAR method based on permanent scatterer (PS) points, proposed by Ferretti et al. [51]. The basic principle of this method is as follows: from the acquired multi-temporal SAR image sequence, an image in the middle is typically selected as the reference master image based on its temporal position, while the remaining images serve as slave images. Subsequently, interferometric pairs are formed by pairing each slave image with the master image, and differential interferometric processing is performed. On this basis, pixels are selected using methods such as amplitude stability analysis to identify permanent scatterer targets with good coherence. Deformation inversion is then carried out based on these targets, ultimately yielding land subsidence information over the study period.

Since PS-InSAR method relies on the phase information of long-term stable scatterers, it is necessary to identify permanent scatterer (PS) points with high coherence from multi-temporal SAR images. For any PS point in a differential interferogram, its interferometric phase is composed of multiple components, including the land subsidence phase, topographic phase, atmospheric delay phase, and noise phase, similar to the SBAS-InSAR time-series InSAR method. After removing the error phases, the land subsidence phase ϕ_{def} is obtained. The conversion relationship between the land subsidence phase and the land subsidence Δr can be expressed as:

$$\Delta r = \frac{\lambda}{4\pi} \cdot \phi_{def} \tag{6}$$

Finally, the time-series land subsidence values and rates for the study area can be obtained.

2.3.3. Coastline Extraction Method

There are various methods for coastline boundary extraction, such as tidal correction, sub-pixel waterline detection, and DSAS-based shoreline change statistics, which are well suited for large-scale coastline mapping [52–56]. However, since the study area in this research covers only approximately 300 km^2—a relatively small extent—this paper adopts simple visual interpretation and the MNDWI (Modified Normalized Difference Water Index) method to extract coastline changes in the study area. The threshold segmentation method is one of the commonly used techniques for extracting coastlines from optical remote sensing imagery [57], and its calculation is as follows:

$$MNDWI = \frac{Green - SWIR}{Green + SWIR} \quad (7)$$

Here, *Green* and *SWIR* represent the reflectance of the green band and the shortwave infrared band of the remote sensing image, respectively. Based on the difference in *MNDWI* values between water and non-water bodies, an appropriate threshold is set to perform binary segmentation on the image, enabling the preliminary extraction of water bodies and generating an initial coastline result. In this study, due to the absence of SWIR bands in the KeyHole panchromatic imagery and Google Earth screen imagery, the MNDWI method was employed solely for shoreline classification using Landsat-8 and Sentinel-2 satellite remote sensing data.

In addition, to improve the accuracy of coastline extraction, the above results are further refined through manual correction using visual interpretation. Misclassified areas caused by factors such as shadows, turbid water, tidal flats, and artificial structures are corrected to ensure the continuity and accuracy of the coastline boundary.

Finally, this paper uses the two methods described above to obtain accurate coastline change results for the study area across different periods, providing reliable foundational data for subsequent analyses of land subsidence and urban stability.

3. Results

This study used 266 scenes of Sentinel-1A SAR data to obtain time-series SBAS-InSAR annual subsidence rate results for the study area from 2016 to 2025. To verify the reliability of the results, this study also employed time-series PS-InSAR to extract annual subsidence rates for the same area from 2016 to 2025 and conducted cross-validation with the SBAS-InSAR results. In addition, this study utilized 44 scenes of optical remote sensing data, including KH, Landsat, and Sentinel-2, to extract annual coastline change results for the study area. On this basis, this study analyzed the spatial distribution characteristics and temporal variation trends of land subsidence.

3.1. Time-Series SBAS-InSAR Land Subsidence Monitoring Results from 2016 to 2025

This study employed time-series SBAS-InSAR to extract annual subsidence rate results for study area from 2016 to 2025, as shown in Figure 4, where red represents subsidence and blue represents uplift. It can be seen from Figure 4 that the land subsidence signal in study area is very pronounced. Temporally, subsidence occurs every year, with the maximum annual subsidence rate reaching -163.53 ± 4.90 mm/yr in 2017. Spatially, there are multiple subsidence areas, mainly located in newly reclaimed areas from the past decade, with some small-scale subsidence areas scattered sporadically in parts of the urban built-up area.

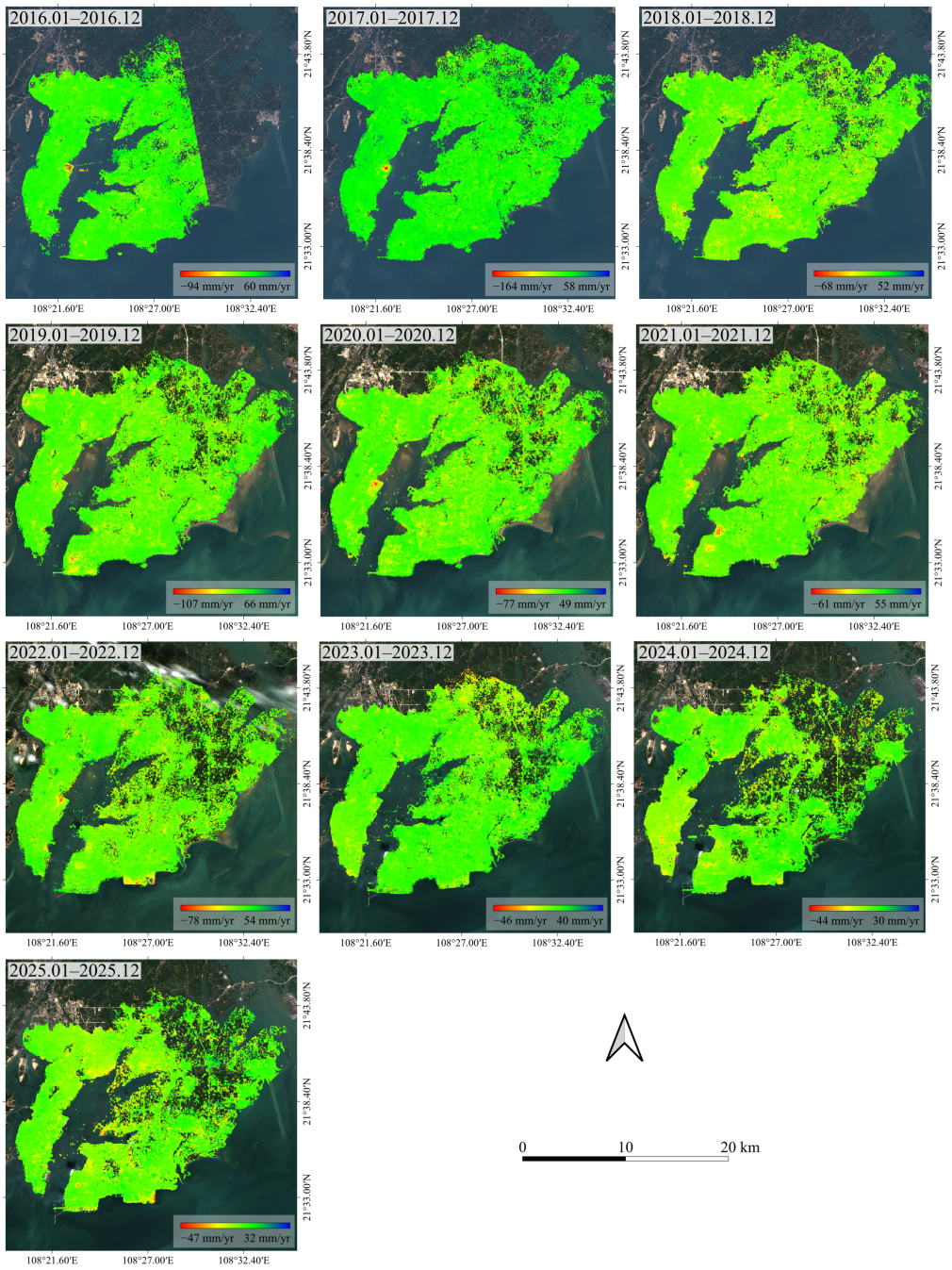


Figure 4. Annual land subsidence rates from time-series SBAS-InSAR over the period 2016–2025.

According to the requirements of the 'Technical Code for Interferometric Radar Data Processing of Land Subsidence (DD2014-11)' [58], the severity of land subsidence areas is classified based on the annual subsidence rate: areas with a subsidence rate lower than −10 mm/yr are classified as stable areas; those with rates between −10 and −30 mm/yr as slow subsidence areas; between −30 and −50 mm/yr as moderate subsidence areas; and those with rates exceeding −50 mm/yr as rapid subsidence areas. This paper conducts a statistical analysis of the land subsidence results derived from time-series SBAS-InSAR over the period 2016–2025, and generates an area proportion map of land subsidence grade classification in the study area, as shown in Figure 5 and Table 2. The figure shows that from 2016 to 2019, the proportions of slow subsidence areas and moderate subsidence areas continuously increased. The main reason is that the area of reclamation continued to increase during this period, leading to an accelerated land subsidence rate. Since 2020,

the proportions of these two types of subsidence areas have been decreasing, while the proportion of stable areas has been increasing year by year. Although new reclamation areas have emerged, a possible reason for this trend is that the previous reclamation areas have been gradually put into use and have undergone consolidation and compaction, causing the subsidence rate to level off, and thus their area proportion has decreased.

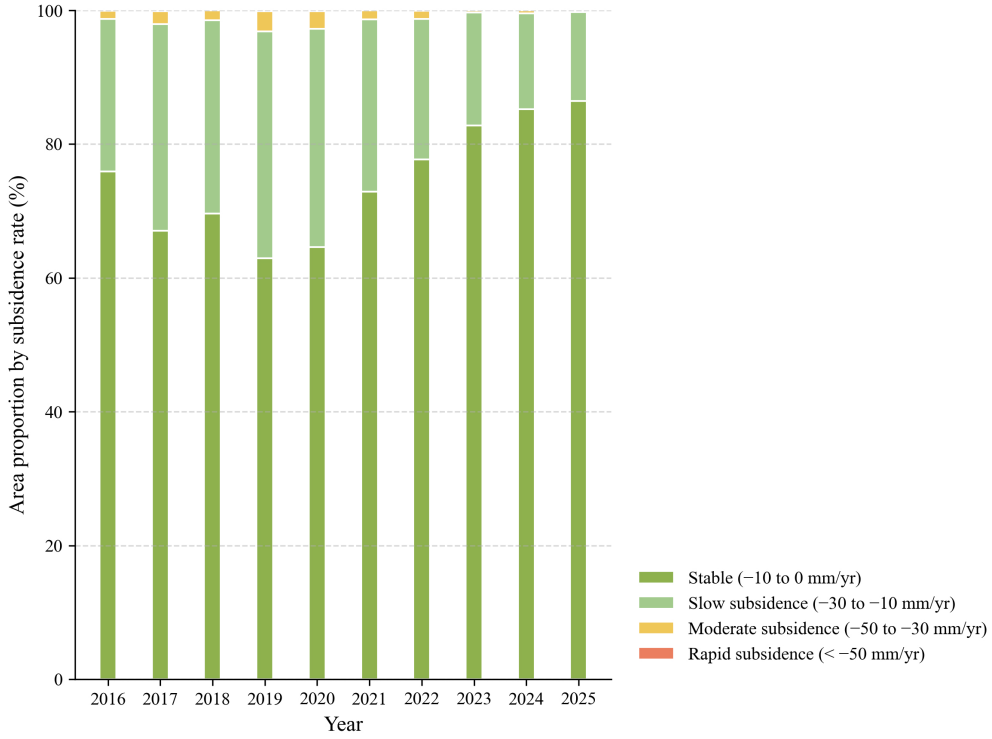


Figure 5. The area proportion of land subsidence grade classification from 2016 to 2025.

Table 2. The area percentages of land subsidence grade classification from 2016 to 2025.

Year	Stable	Slow Subsidence	Moderate Subsidence	Rapid Subsidence
2016	75.89	22.82	1.17	0.12
2017	67.01	30.89	1.93	0.17
2018	69.62	28.89	1.44	0.05
2019	62.95	33.88	2.98	0.19
2020	64.6	32.59	2.66	0.15
2021	72.89	25.76	1.3	0.05
2022	77.71	20.96	1.24	0.09
2023	82.76	16.85	0.38	0.01
2024	85.21	14.34	0.42	0.03
2025	86.44	13.28	0.27	0.01

3.2. Time-Series PS-InSAR Land Subsidence Monitoring Results and Cross-Validation

To verify the accuracy of the land subsidence results obtained from time-series SBAS-InSAR, this study also employed time-series PS-InSAR to monitor land subsidence. After performing time-series PS-InSAR processing on the Sentinel-1A data covering the study area for 2025, a land subsidence rate map for 2025 was generated using time-series PS-InSAR. This result was then compared and displayed alongside the time-series SBAS-InSAR land subsidence rate for 2025, as shown in Figure 6. By comparing the land subsidence monitoring results from the two methods, it was found that the spatial distribution of subsidence derived from the two time-series InSAR methods is highly consistent. However, since time-series PS-InSAR relies on persistent scatterers that maintain stability and high

quality over long time series, it is difficult to obtain high-quality PS points in reclaimed coastal areas where surface changes occur rapidly. As a result, the PS points in the time-series PS-InSAR results are relatively sparse compared to those in the time-series SBAS-InSAR results.

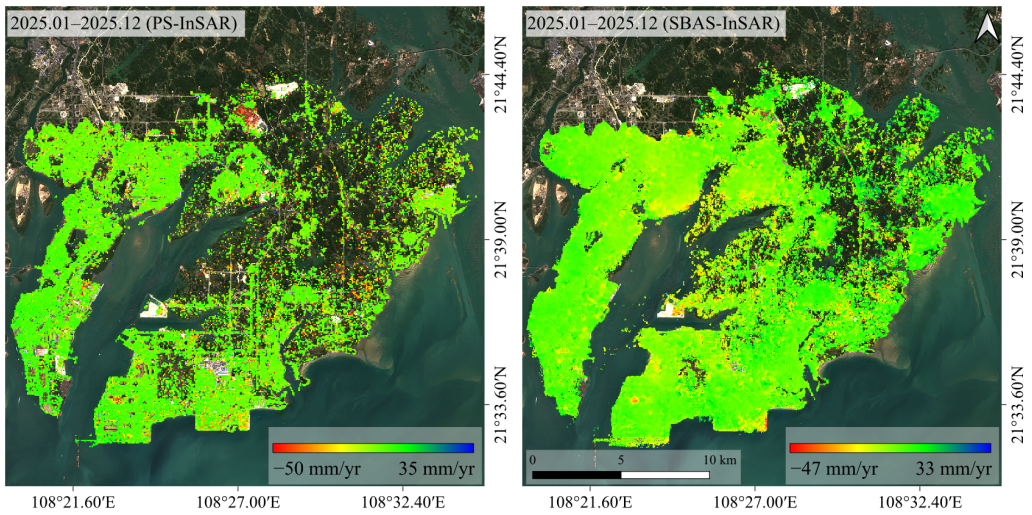


Figure 6. Comparison of land subsidence rate from PS-InSAR and SBAS-InSAR in 2025.

To further verify the correlation between the two time-series InSAR results, we selected four different ground points as validation points from the 2025 cumulative land subsidence results of PS-InSAR and SBAS-InSAR for result comparison. The spatial distribution of the validation points is shown in Figure 7.

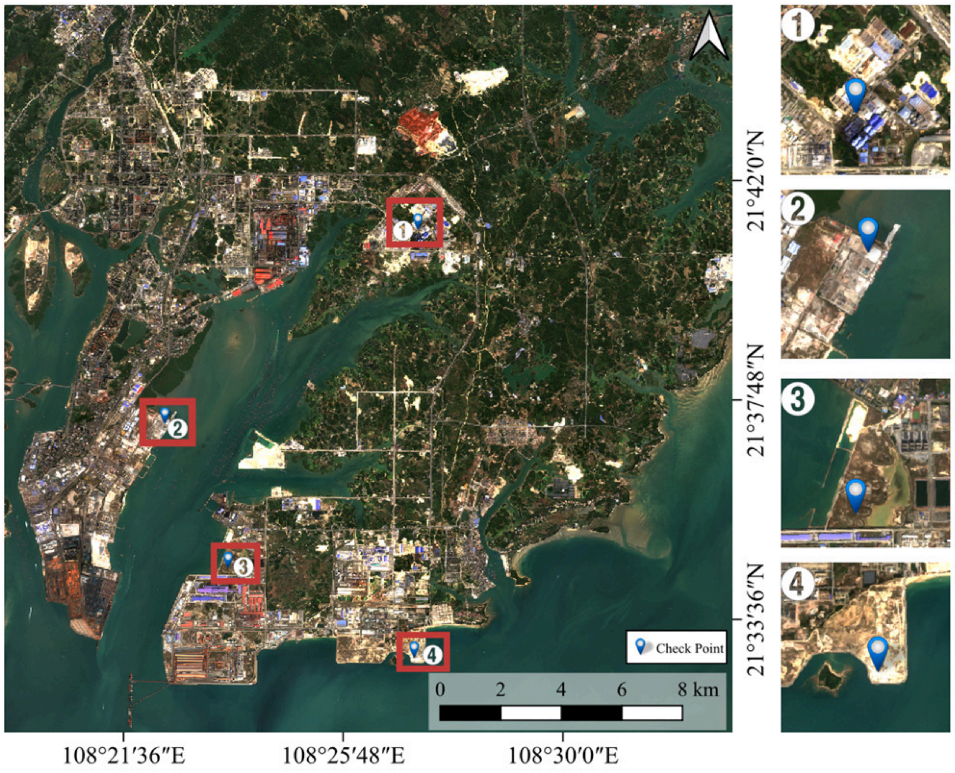


Figure 7. Spatial distribution map of the four validation points.

Figure 8 shows the comparison of the time-series land subsidence between PS-InSAR and SBAS-InSAR at the four validation points in 2025. It can be seen from Figure 8 that the subsidence trends presented by the two land subsidence monitoring results are highly consistent. The RMSE values of the land subsidence trends calculated for the four validation points are all less than 4 mm. From the fitted trend lines of PS-InSAR and SBAS-InSAR, it can be observed that there is a systematic error of approximately 2 mm between the two land subsidence results at validation points 3 and 4. The possible reason for this error may be the difference in surface features—that is, around validation points 3 and 4, there are fewer buildings, leading to relatively sparse stable and reliable PS points. However, overall, the two land subsidence results maintain a high degree of consistency both spatially and temporally. This cross-validation can indicate that the time-series InSAR land subsidence monitoring results presented in this paper are reliable.

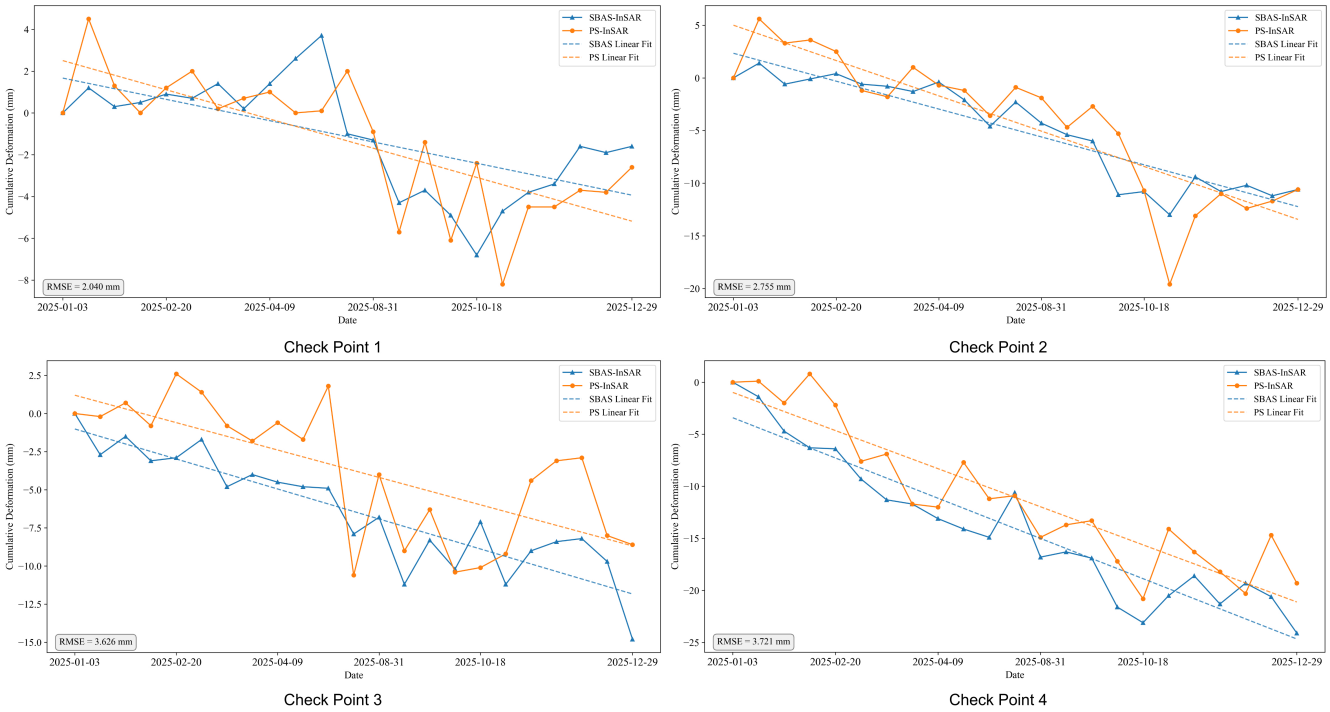


Figure 8. Comparison of land subsidence results between PS-InSAR and SBAS-InSAR in 2025.

3.3. Annual Coastline Change Results of Fangchenggang City from 1964 to 2025

This study utilizes 44 scenes of optical remote sensing imagery, including declassified U.S. military reconnaissance KeyHole satellite images, Google Earth historical imagery, Landsat 8 OLI images, and Sentinel-2A MSI images. Using the MNDWI threshold method and visual interpretation method, annual coastline changes map of the study area from 1964 to 2025 were generated, as shown in Figure 9. Figure 9 reveals that since 1964, the coastline of Fangchenggang City has undergone significant changes, with large-scale reclamation projects on the Yuwan Peninsula and the Qisha Peninsula, leading to a marked expansion of artificial coastlines. Notably, reclamation on the Yuwan Peninsula has been ongoing continuously since 1964, with newly added reclaimed areas almost every year. Compared with the land area of the Yuwan Peninsula in 1964, its land area in 2025 has increased by approximately twofold. In contrast to the Yuwan Peninsula, the Qisha Peninsula experienced relatively little reclamation before 2008, but has since undergone large-scale reclamation projects, especially in recent years.

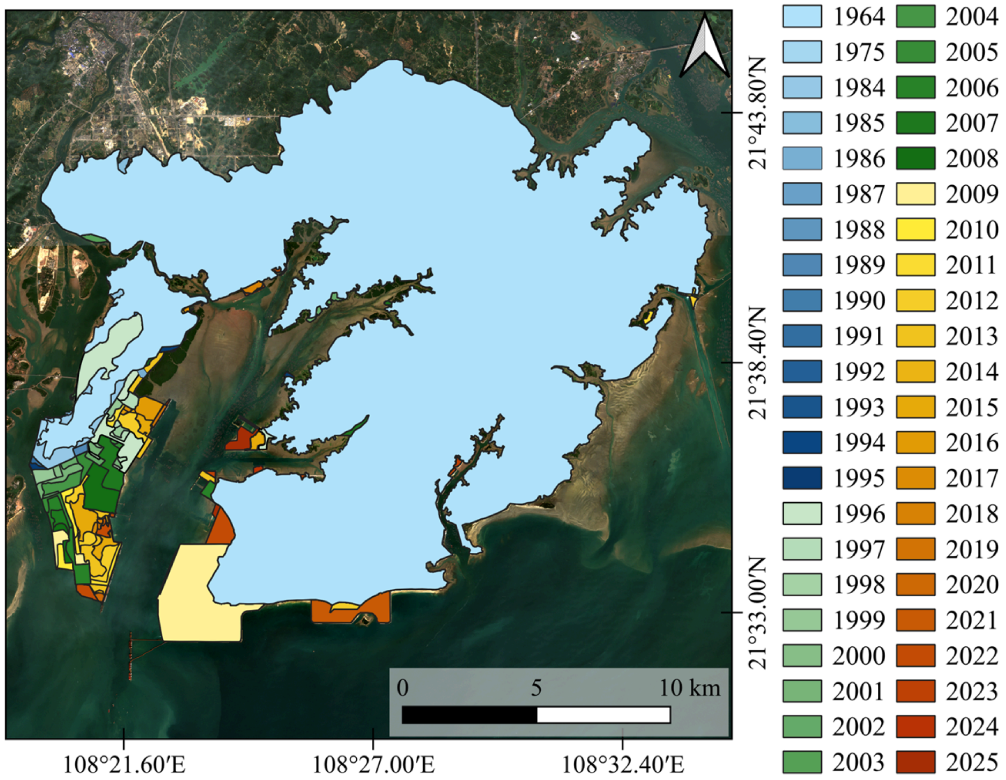


Figure 9. Coastline changes map of the study area from 1964 to 2025.

3.4. Spatiotemporal Distribution Characteristics of Land Subsidence

Based on the time-series SBAS-InSAR land subsidence results in Figure 4 and the coastline changes in Figure 9, seven major land subsidence areas (Area A-G) were identified, and their spatial distribution is shown in Figure 10. Since 2016, subsidence began to occur in Areas A, B, and C. Subsidence in Area D began in 2019. During the period of 2016–2019, Areas A, B, and C continued to experience persistent subsidence, but the overall subsidence rates showed a decelerating trend. From 2022 onwards, subsidence began in Areas E and F. Area G also started to subside from 2025. Hence, there are seven distinct land subsidence areas in the study area, and the maximum land subsidence rate exhibits a decelerating trend over time. It is worth noting that these land reclamation areas exhibit predominantly negative deformation signals (i.e., subsidence), with virtually no positive deformation signals. This absence of positive signals persists even in areas where engineering activities, such as building construction, have increased the ground elevation. The underlying reason is that the elevation changes caused by these construction activities severely degrade the coherence of the InSAR interferometric pairs. Because we excluded low-quality interferometric pairs during data processing, the corresponding positive deformation signals were consequently filtered out.

To more clearly present the temporal trends of the reclamation areas, we selected four areas (A–D) with long time-series data, using one representative point per area, to illustrate the temporal subsidence characteristics over the past decade (Figures 11–14). The results show that land subsidence in all four reclamation areas has been continuously decreasing. In particular, Areas A, C, and D exhibit a pattern of “rapid decrease in the early stage, followed by a slower decrease”.

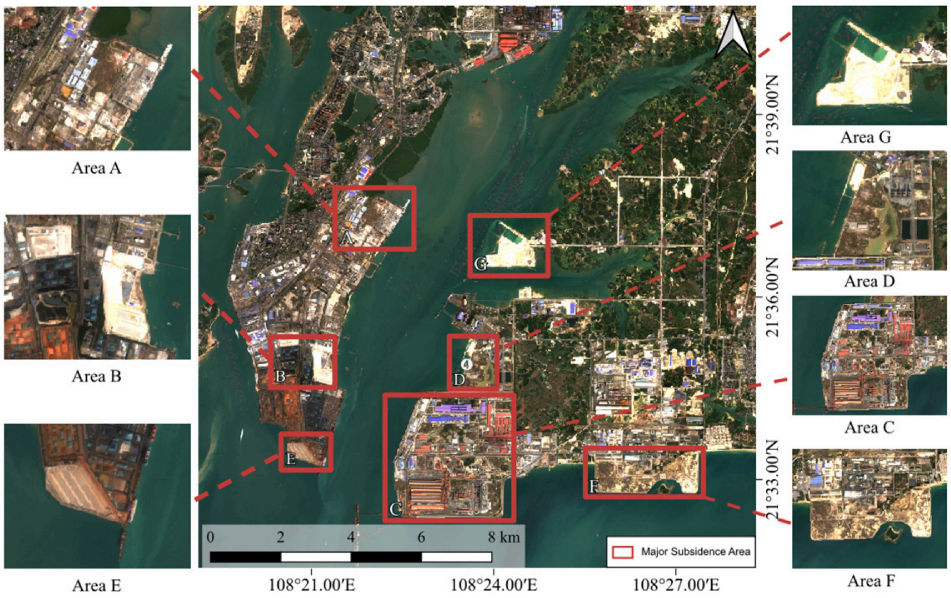


Figure 10. Spatial distribution of seven major subsidence areas (Area A–G).

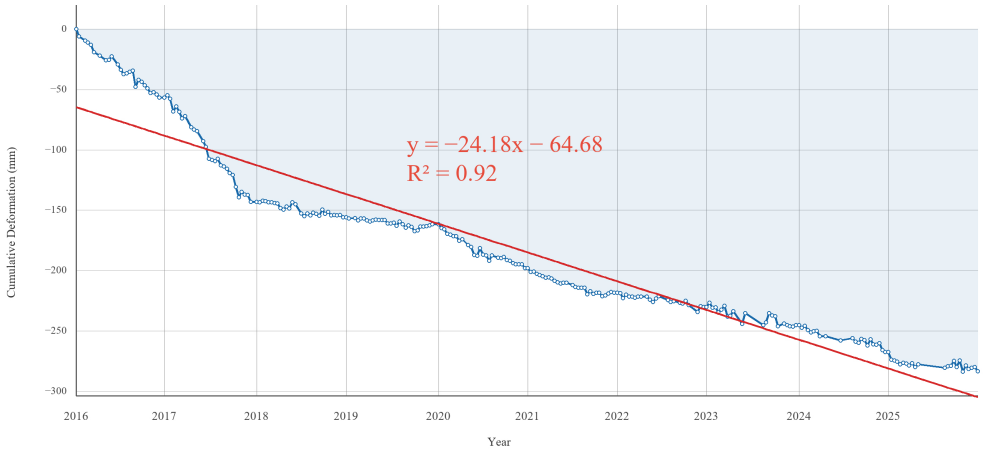


Figure 11. Cumulative deformation time-series curve for region A.

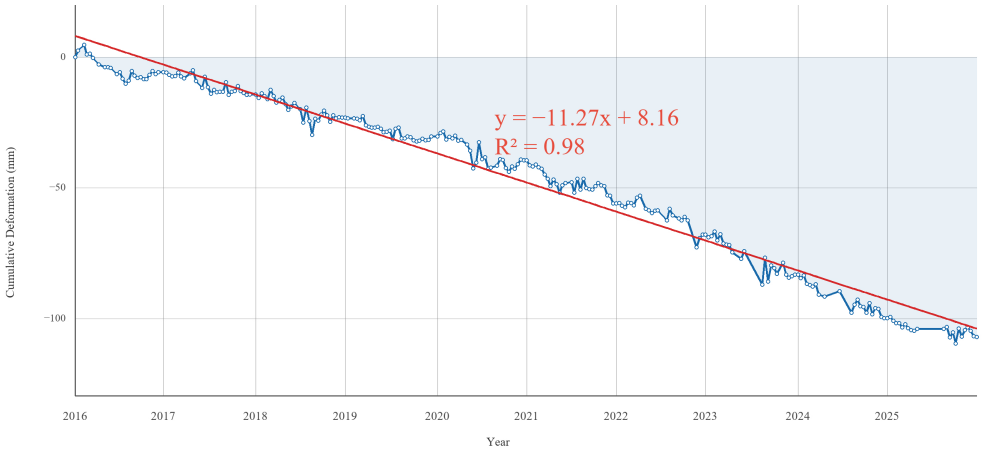


Figure 12. Cumulative deformation time-series curve for region B.



Figure 13. Cumulative deformation time-series curve for region C.



Figure 14. Cumulative deformation time-series curve for region D.

3.5. Temporal Variation Trends of the Seven Main Subsidence Areas

To further analyze the temporal trends of land subsidence in the seven main areas, this paper presents the annual land subsidence rates for each area in detail, as shown in Figures 15–21.

Area A refers to Berths 513–516 of Fangchenggang Port. Berth 513 is a 30,000-ton multi-purpose berth, while Berths 514–516 are 30,000-ton general-purpose berths, with a total tonnage of 120,000 tons. The total length of the wharf coastline is 1002 m, and the underwater excavation area is 9.12 million m^2. The land reclamation for Area A was carried out from 2015 to 2019. It was put into trial operation in early 2020 and officially opened to traffic in 2025. As shown in Figure 15, during the initial stage of reclamation, Area A exhibited a pronounced funnel-shaped subsidence zone. Over time, the intensity of the subsidence center weakened, the spatial gradient became gentler, and the pattern gradually transitioned from a funnel shape to dispersed areal subsidence. By 2023–2025, only slight residual subsidence remained, and the original funnel shape had largely disappeared. The primary reason for the above phenomenon is that reclamation is the dominant factor driving land subsidence, while engineering activities such as wharf construction and operation have a detectable but less pronounced influence. According to the SBAS-InSAR results, Area A experienced the maximum land subsidence rate in 2017, reaching up to -163.53 ± 4.90 mm/yr.

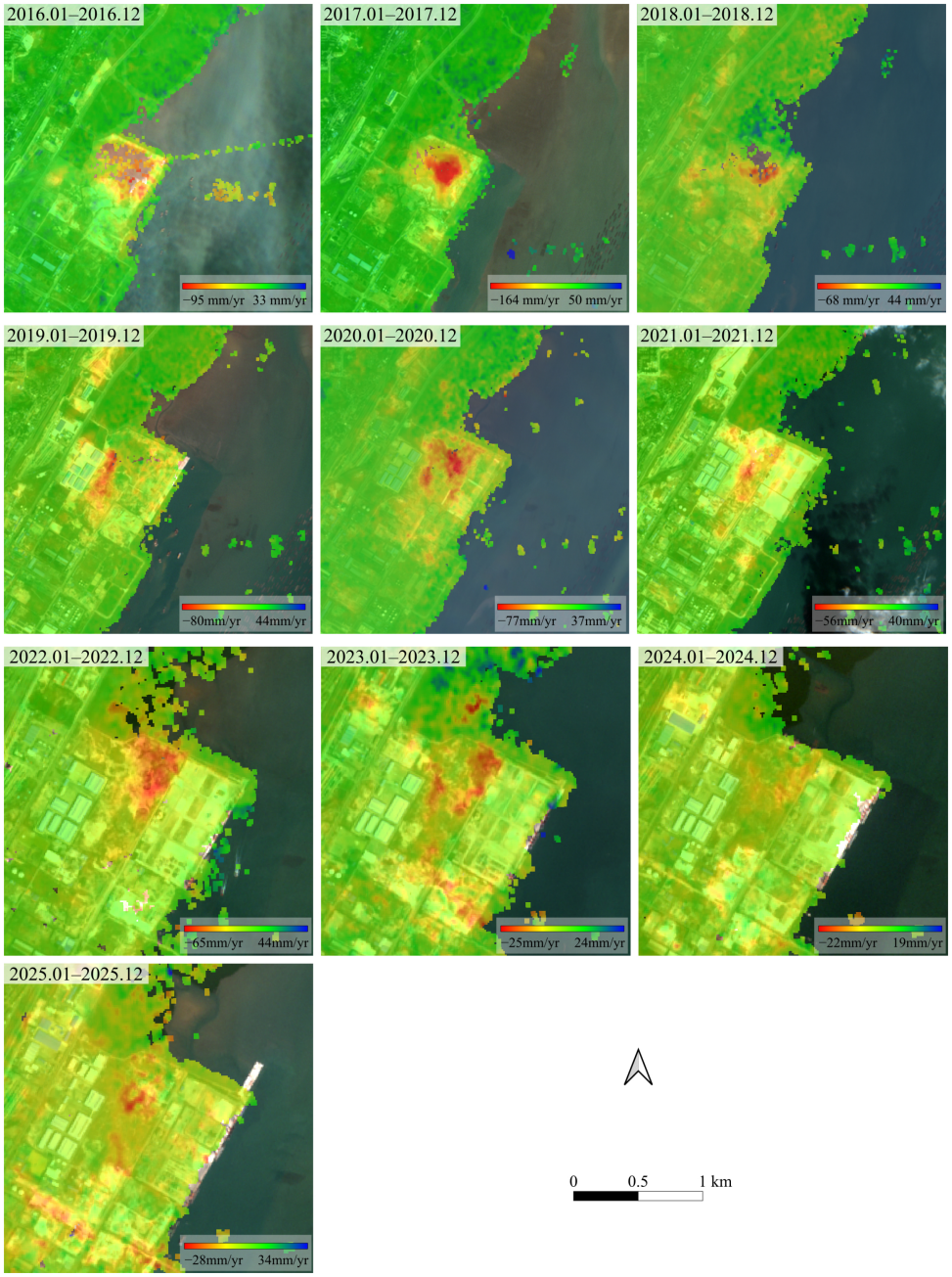


Figure 15. The temporal trend of land subsidence at Berths 513–516 of Port (Area A).

Area B is the reclamation area around the Fangchenggang coal storage base and Zhongchu Road. The reclamation project in this area was carried out from 2014 to 2018. Construction of the Fangchenggang Coal Storage Base began on 27 September 2022, and it was put into operation in 2025, covering an area of approximately 0.37 km^2. The base is mainly used to receive and store discharged materials from specialized berths 401# and 20–21#, as well as to meet the demands of transporting stockpile materials by train, truck, and water transfer. As shown in Figure 16, this area primarily exhibits uneven areal subsidence. From 2016 to 2018, the extent of the subsidence area continued to expand. From 2019 to 2021, with the completion of the reclamation works, the land subsidence rate slowed down, and the area of high subsidence rates decreased correspondingly. The primary cause of the above phenomenon is that reclamation remains the dominant factor driving land subsidence. Even in 2024, following the coal storage engineering activities, the subsidence areas are still situated on bare land. After the project was completed in 2025, the

subsidence rate slowed down. According to the SBAS-InSAR results, Area B experienced the maximum land subsidence rate in 2022, reaching up to -59.77 ± 3.62 mm/yr.

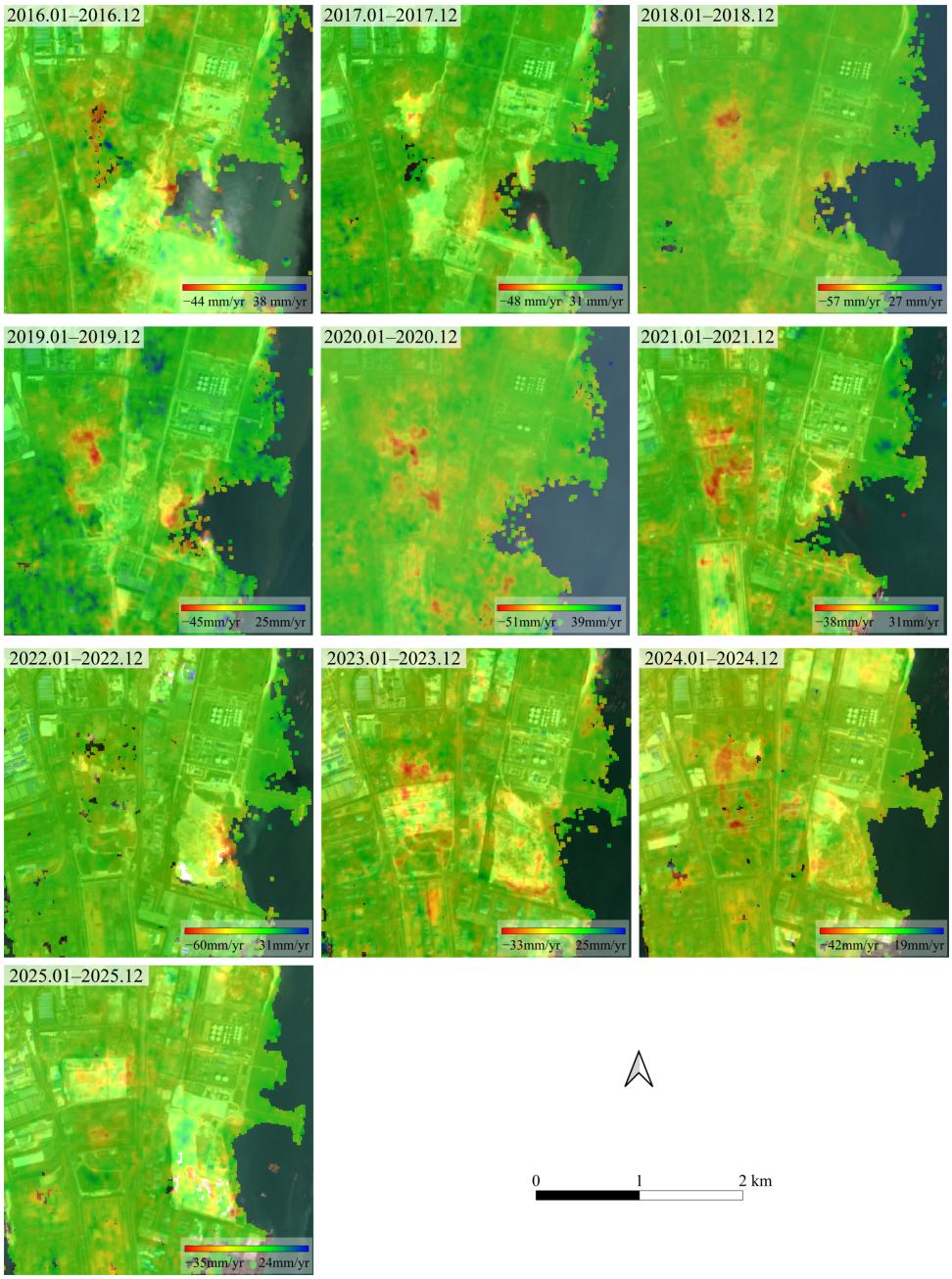


Figure 16. The temporal trend of land subsidence at the Coal Storage Base (Area B).

The reclamation project in area C was carried out between 2008 and 2011, and construction began in 2012. The base is now in operation, though construction work is still ongoing. As shown in Figure 17, in 2019, relatively pronounced land subsidence occurred, predominantly on bare land, and gradually decreased thereafter. Reclamation remains the primary factor driving this subsidence. According to the SBAS-InSAR results, Area C experienced the maximum land subsidence rate in 2019, reaching up to -107.23 ± 8.25 mm/yr.

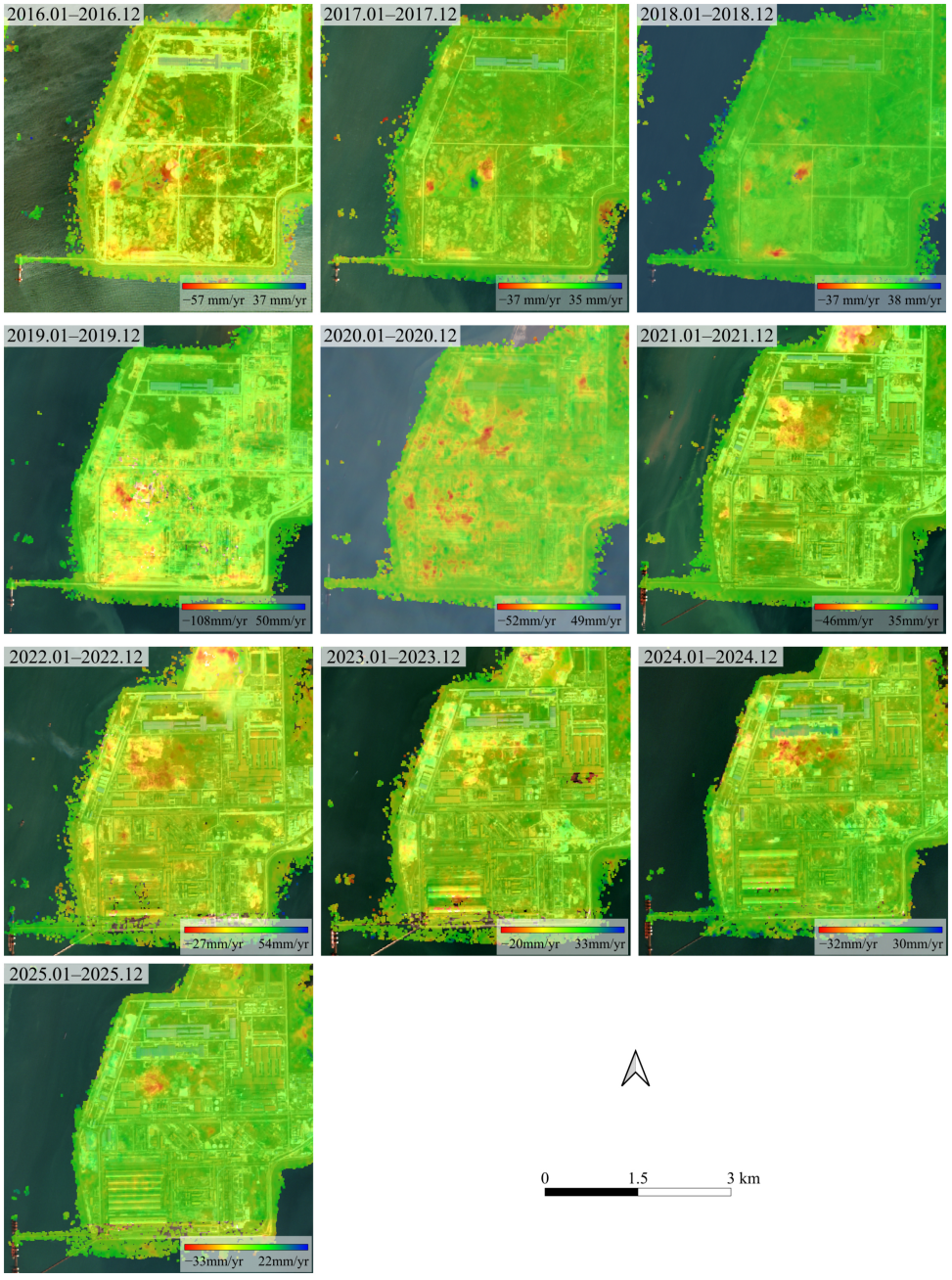


Figure 17. The temporal trend of land subsidence at the Fangchenggang Base of Guangxi Iron and Steel Group (Area C).

Area D is the reclaimed area around Guangxi Mingyang Smart New Energy Technology Co., Ltd. The reclamation project began in 2020 and has not yet been completed, and it is still under construction. This area is planned to be developed into the Qisha Offshore Wind Power Equipment Manufacturing Base. As shown in Figure 18, the reclamation in this area involves constructing embankments first, with the reclamation works proceeding sequentially from the coastal zone inland. Slight land subsidence began to appear in 2020, and a significant subsidence funnel emerged in 2021, indicating a very clear signal of land subsidence. After 2021, the land subsidence in this area gradually slowed down and exhibited uneven areal characteristics. Based on the locations where subsidence occurred, the above land subsidence is primarily attributable to reclamation, with engineering activities playing a relatively minor role. According to the SBAS-InSAR results, Area D experienced the maximum land subsidence rate in 2020, reaching up to -70.22 ± 5.72 mm/yr.

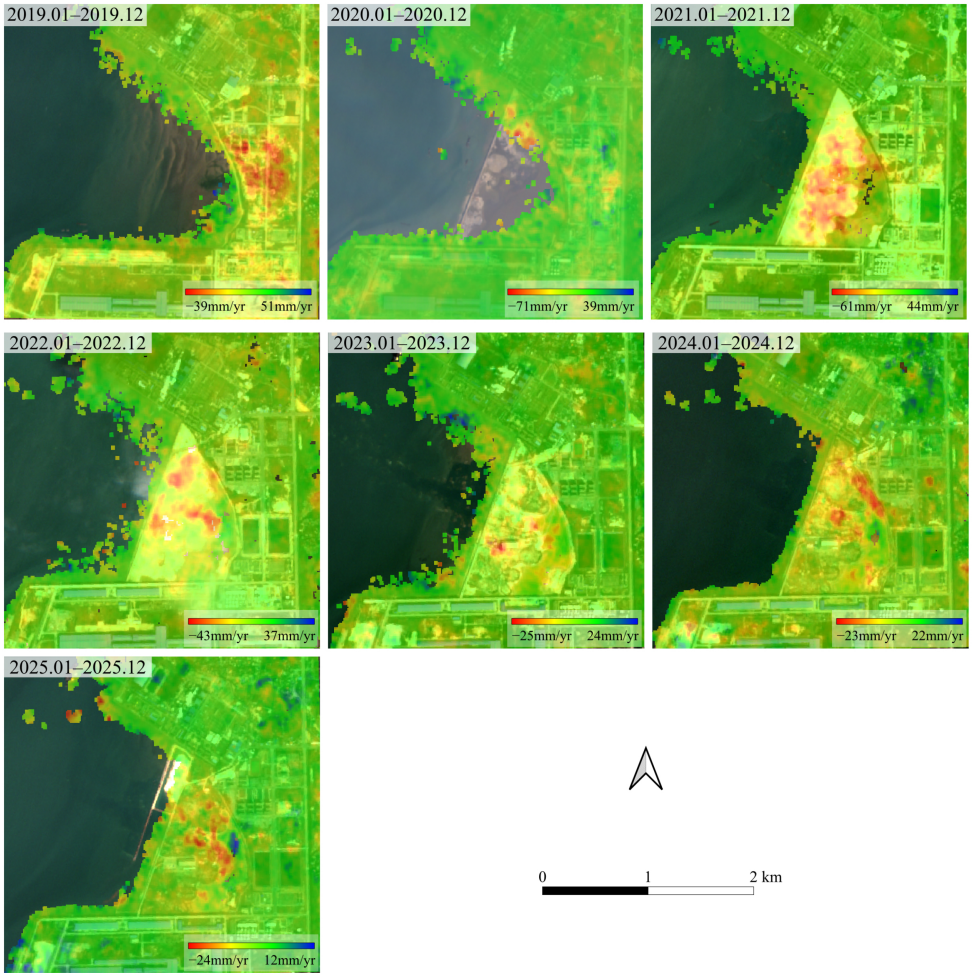


Figure 18. The temporal trend of land subsidence around the Guangxi Mingyang Smart New Energy Technology Co., Ltd. (Area D).

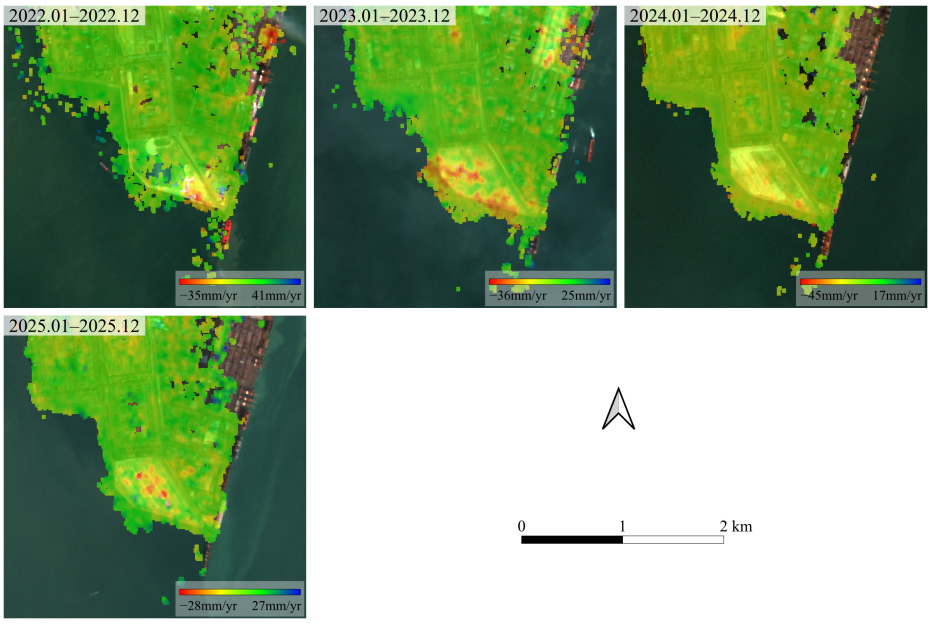


Figure 19. The temporal trend of land subsidence at the Berth 401# (Area E).

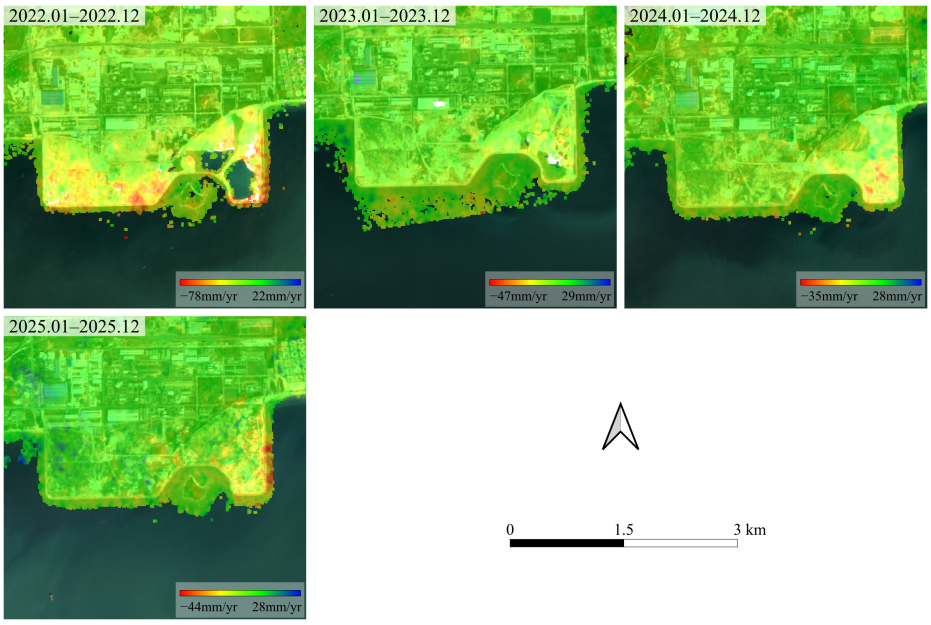


Figure 20. The temporal trend of land subsidence around the Guangxi Jinchuan Nonferrous Metals Co., Ltd. (Area F).

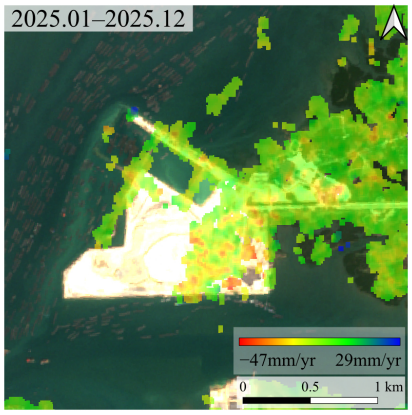


Figure 21. The temporal trend of land subsidence around the Fangchenggang Yuzhiyuan Sea Fishing Club (Area G).

Area E is the second-phase project of Berth 401# at Fangcheng Port, covering an area of nearly 0.334 km^2. The reclamation of this area was carried out between 2022 and 2023, and has since been completed. Currently, the area is in the initial construction stage for the port's bucket-wheel stacker-reclaimer and belt conveyor systems. As shown in Figure 19, the subsidence in this area is predominantly characterized by uneven areal subsidence, with a spatial pattern of strong subsidence in the center and weaker subsidence at the margins. The most significant land subsidence occurs in the central part of the reclaimed area, away from the coastline protection structures, while the peripheral areas near the existing quay walls and temporary construction roads remain relatively stable. According to the SBAS-InSAR results, Area E experienced the maximum land subsidence rate in 2024, reaching up to -44.55 ± 5.41 mm/yr.

Area F is the reclaimed area around Guangxi Jinchuan Nonferrous Metals Co., Ltd. This area is part of the first phase of the Series II nickel-iron smelting project, with a reclamation area of 0.27 km^2. The reclamation was carried out between 2021 and 2024. As shown in Figure 20, the reclamation works in this area progressed spatially from west to east, and this movement pattern is consistent with the spatial evolution of land subsidence

observed by time-series InSAR. In 2022, the western reclaimed area experienced a relatively high subsidence rate and a larger spatial extent of land subsidence, while land subsidence in the eastern part was mainly concentrated along the embankment areas. By the end of 2022, reclamation in the western part of the area was largely completed. In 2023, partial reclamation works were carried out in the eastern area, though not yet fully completed. By 2024, reclamation in the eastern part of the area was essentially finished. According to the SBAS-InSAR results, Area F experienced the maximum land subsidence rate in 2022, reaching up to -77.64 ± 10.00 mm/yr.

Area G is the reclaimed area around the Fangchenggang Yuzhiyuan Sea Fishing Club, as shown in Figure 21. Due to the impact of the reclamation project, land subsidence occurred in this area in 2025. According to the industrial spatial layout plan of Fangchenggang City published by the Fangchenggang Natural Resources Bureau, additional reclamation works are planned for this area in the future. The SBAS-InSAR results show that the maximum land subsidence rate in Area G reached -46.97 ± 4.53 mm/yr in 2025.

In the subsidence areas described above, we observed that subsidence mainly occurs in reclaimed land, especially where subsidence values become negligible after construction activities such as building construction. The main reason may be that the underlying loose fill has already undergone primary consolidation under its own weight (or preloading) by the time construction begins. While it might seem intuitive that heavier buildings would induce more subsidence, in this case, the additional load from the superstructure actually accelerates the consolidation of deeper foundation soils. Furthermore, where pile foundations are used, building loads are transferred to deeper, high-capacity bearing layers, decoupling the upper structure from the shallow consolidation subsidence of the surrounding reclaimed areas. This accounts for why the completed structures exhibit much less apparent deformation compared to the surrounding untreated fill.

The parameters for Areas A–G, including reclamation area, reclamation period, current land use, maximum subsidence rate, and the corresponding year of occurrence, have been summarized and are presented in Table 3.

Table 3. The parameters related to reclamation for Areas A–G.

Reclamation Area Code	Reclaimed Area	Reclamation Period	Current Land Use	Maximum Rate (mm/yr) and Its Year
Area A	1.45 km^2	2015–2019	Port and bare land	-163.53 ± 4.90/2017
Area B	1.70 km^2	2014–2018	Industrial and bare land	-59.77 ± 3.62/2022
Area C	9.29 km^2	2008–2011	Industrial and bare land	-107.23 ± 8.25/2019
Area D	1.06 km^2	2020–present	Industrial and bare land	-70.22 ± 5.72/2020
Area E	0.31 km^2	2022–2023	Port and bare land	-44.55 ± 5.41/2024
Area F	2.14 km^2	2021–2024	Industrial and bare land	-77.64 ± 10.00/2022
Area G	1.02 km^2	2025–present	Bare land	-46.97 ± 4.53/2025

4. Analysis and Discussion

The factors influencing land subsidence are multifaceted and complex, typically attributable to two major categories: human and natural factors. Human factors include activities such as land reclamation. Natural factors such as precipitation and changes in groundwater levels also affect urban stability.

4.1. Land Reclamation Factor

As shown in Figure 22, the land area has exhibited a gradual increasing trend since 1964, following a "three-stage" growth pattern: 1964–1995, 1995–2008, and 2008–2025. During the period from 1964 to 1995, land area growth was relatively slow. However, in

1997, a relatively large-scale reclamation project was carried out on the Yuwan Peninsula, and from then until 2008, land area growth accelerated. In 2010, another large-scale reclamation project occurred on the Qisha Peninsula, and from then until 2025, land area growth further accelerated. In 1964, the total area of the study region was 276.29 ± 0.37 km^2, which increased to 316.11 ± 1.47 km^2 by 2025, representing an increase of approximately 39.82 ± 1.52 km^2. From 1964 to 1995, the land area increased relatively slowly, with a net increase of only 2.23 ± 4.51 km^2 and a growth rate coefficient of 0.06. During the period from 1995 to 2008, the land area increased significantly, expanding by 14.28 ± 6.19 km^2 with a growth rate coefficient of 0.78. From 2008 to 2025, the increase in land area became even more pronounced, with a net increase of approximately 23.31 ± 4.51 km^2 and a growth rate coefficient of 1.01. This growth trend reflects the entire development process of land area expansion in the study area.

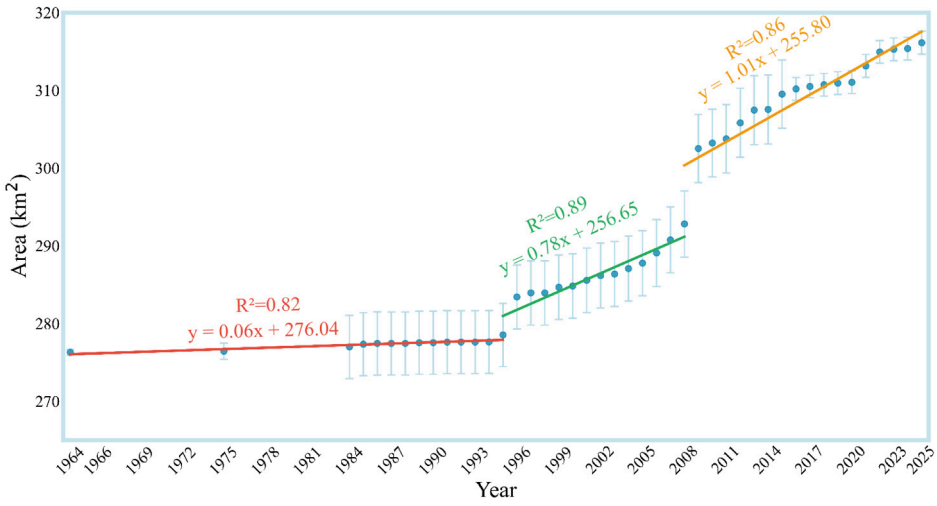


Figure 22. Changes in land area of the study area from 1964 to 2025.

The increase in land area is attributed to multiple factors, including geological conditions, reclamation methods, and urban construction. First, the offshore sediments are predominantly composed of loose, low-strength silt and clay. Due to sedimentation, a thick soft soil layer has formed in the offshore area, which has contributed to the increase in land area [18,24,59]. However, this geological condition has poor bearing capacity and is prone to land subsidence. Second, a combination of reclamation methods—namely, mountain excavation and sand filling, as well as hydraulic sand filling—has further reduced the bearing capacity of the reclaimed land foundation, due to the influence of the soft soil layer and underlying silt in the reclamation area. For example, the large-scale artificial land reclamation at the southeastern tip of the Yuwan Peninsula has altered tidal currents throughout the bay, resulting in a significant increase in sedimentation in the study area in recent years. Third, on the east side of the Xiwan Cross-Sea Bridge, northwest of the Yuwan Peninsula, the construction of expressways and high-speed railways has blocked the bay inlet, causing a marked reduction in the water area of Xiwan Bay. According to the interannual coastline change results shown in Figure 9 and the time-series InSAR land subsidence monitoring results from 2016 to 2025 shown in Figure 4, all seven major subsidence areas (Areas A–G) during this period are located in reclaimed zones. Therefore, land reclamation has been the primary means of land area expansion. Land reclamation typically involves processes such as cofferdam construction, hydraulic filling, land subsidence, and soft ground treatment. Among these, land subsidence is an unavoidable issue. Land subsidence caused by the compaction of the fill layer generally tends to stabilize after more than 20 years, during which the ground will experience continuous and slow subsidence [24].

The degree of land subsidence in reclaimed areas also varies, primarily depending on land use, such as building construction and the use of heavy machinery and equipment [18,59]. The factors inducing land subsidence in Areas A and E are mainly the frequent use of heavy machinery and equipment, the storage of large quantities of coal, ore, and other goods, and dense traffic flow, all of which exert tremendous pressure on the ground, further promoting soil consolidation and compression, resulting in significant land subsidence. Area B is the Fangchenggang Coal Storage Base, where the main factor contributing to land subsidence is the use of heavy machinery and equipment during the construction of the storage base. Areas D and F are in the late stages of reclamation projects, with no ground engineering construction having yet taken place. The primary cause of land subsidence in these areas is the creep of loose reclaimed materials, such as soft soil particles, under their own weight, leading to gradual compaction and slow compression consolidation of the soil layers, which in turn results in land subsidence. Area C underwent reclamation works during 2008–2011; therefore, the causes of land subsidence during this period were similar to those in Areas D and F. During 2019–2020, the Guangxi Iron and Steel Group Fangchenggang Base constructed a large number of factory buildings and related production facilities in Area C. This engineering construction promoted the compression and consolidation of the fill materials. As shown in the land subsidence monitoring results in Figure 4, land subsidence in 2019 was more severe than in other years. During 2021–2023, factory construction continued in the northern part of Area C, where subsidence remained more severe compared to the central and southern parts. Additionally, Area G is a newly reclaimed area in 2025. As shown in the land subsidence monitoring results in Figure 4, with the launch of a new round of reclamation works in 2025, significant land subsidence occurred in the reclaimed Area G.

4.2. Precipitation Factor

Precipitation is also an important factor affecting land subsidence. The study area is adjacent to the Beibu Gulf. Under the influence of the tropical monsoon climate and maritime air masses, the climate in this area is characterized by being hot and humid with abundant rainfall, as well as distinct alternations between drought and flood. Therefore, during the dry season, the land subsidence rate in the area is relatively high, while during the rainy season, the subsidence rate slows down and even exhibits small-scale rebound fluctuations. To analyze the relationship between land subsidence and precipitation in the study area, three ground points were selected within the study area, among which Point 1 and Point 3 are located in non-reclamation areas, while Point 2 is located in a reclamation area. Their spatial locations are shown in Figure 23. This paper obtained monthly precipitation data for 2022 from the Department of Water Resources of Guangxi and the Statistics Bureau of Guangxi. The annual precipitation is approximately 2000 mm, with precipitation peaks occurring in February, June, August, and October, as shown in Figure 24. The time-series InSAR land subsidence results for these three ground points in 2022 were extracted and overlaid with the monthly precipitation data for 2022, as presented in Figure 23. Through comparison, it was found that the time-series land subsidence at the Point 1 and Point 3 in 2022 exhibited a slightly fluctuating downward trend. These slight fluctuations mainly occurred during the precipitation peak months of February, June, August, and October. Specifically, when precipitation increased, the land subsidence values in the study area showed a rebound phenomenon; when precipitation decreased, the land subsidence values normally declined. The main reason for this may be that the amount of precipitation affects groundwater recharge and soil moisture conditions, thereby indirectly influencing the land subsidence values.

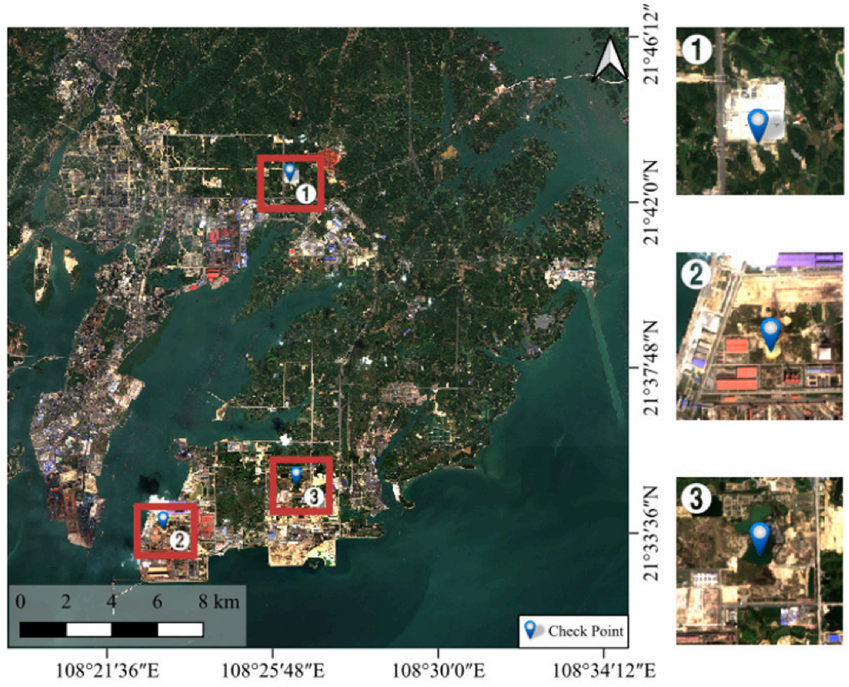


Figure 23. The spatial locations of the three ground points.

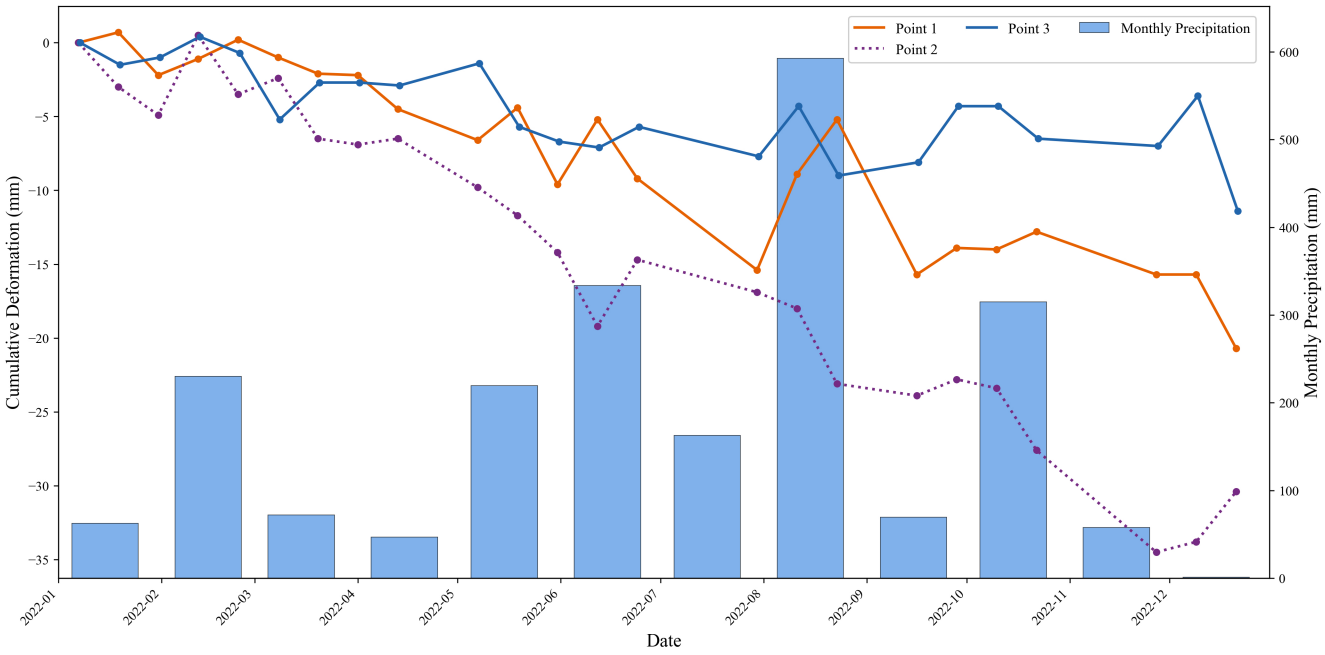


Figure 24. Relationship between monthly precipitation and time-series land subsidence.

4.3. Groundwater Storage Changes Factor

Changes in groundwater storage are also a factor influencing land subsidence, meaning that the recovery of groundwater storage helps reduce the rate and intensity of land subsidence. This study obtained the annual groundwater storage data for the study area from 2016 to 2024 from the Water Resources Department of Guangxi and the Statistics Bureau of Guangxi, and overlaid these data with the annual maximum land subsidence rates, as shown in Figure 25. It can be seen from Figure 25 that in recent years, the groundwater storage in Fangchenggang City has shown an overall fluctuating upward trend—that is, as groundwater storage increases, the maximum land subsidence rate

exhibits a decreasing trend. We calculated the correlation between land subsidence rate and groundwater change, and they show a certain degree of correlation.

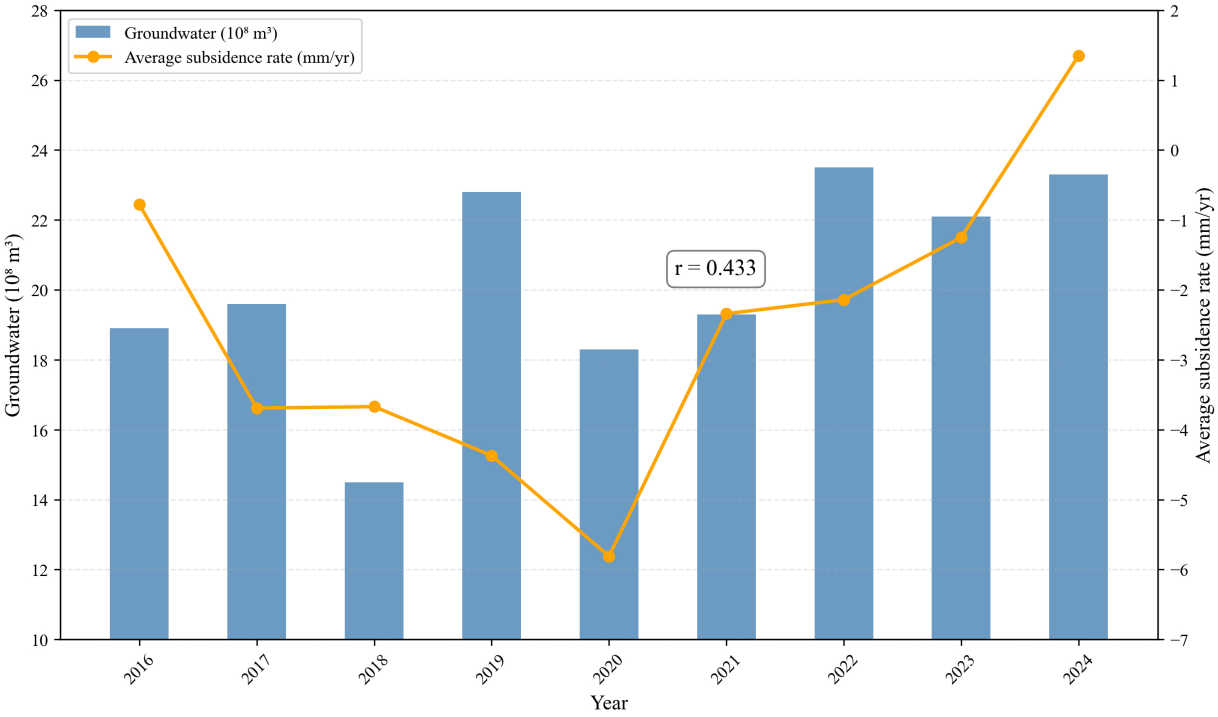


Figure 25. The relationship between changes in groundwater storage and the annual maximum land subsidence rate.

4.4. Comparison with Previous Studies

(1) Interpretation. Based on 266 Sentinel-1A SAR images (2016–2025) and SBAS-InSAR time-series analysis, this study identified seven distinct land subsidence funnels in Fangchenggang City, with maximum rates reaching -163.53 ± 4.90 mm/yr. Coastline change analysis from 1964 to 2025 revealed that coastal reclamation is the dominant driver of land subsidence, while precipitation and groundwater play secondary roles.

(2) Comparison with previous studies. The results of this study were also compared with previous research. In 2024, Luo et al. utilized PS-InSAR technology to monitor time-series land subsidence in Beibu Gulf cities including Fangchenggang, Qinzhou, and Beihai, and conducted factor analysis [32]. Due to the high coherence requirement of PS-InSAR, the resulting deformation points were extremely sparse, particularly in Gangkou District of Fangchenggang, where points were so scarce that subsidence funnel signals could not be identified at all—especially in the reclaimed coastal zones, where almost no monitoring points were available. This limitation stems from an inherent drawback of PS-InSAR, which demands high-coherence targets. Although Gangkou District of Fangchenggang is an urban area, the reclamation zones were initially dominated by bare land, with very few high-coherence features such as buildings and large equipment. Despite failing to identify subsidence funnel signals in the reclamation zones of Gangkou District, that study nevertheless provided a conceptual framework for cross-validating SBAS-InSAR and PS-InSAR results, offering a solution to the lack of field validation in our study. In 2024, Ming et al. employed SBAS-InSAR technology to extract time-series subsidence results for Fangchenggang and Qinzhou from 2018 to 2021 [33]. Benefiting from the dense point coverage advantage of SBAS-InSAR, their results clearly depicted the subsidence patterns in Fangchenggang. However, upon examining these subsidence results, we identified a suspected systematic trend error from Fangcheng District to Gangkou District (i.e., from

north to south): Fangcheng District exhibited almost no subsidence signals, while the entire Yuwang Peninsula in Gangkou District was shown as a subsiding zone. Such a spatial distribution pattern is geologically unreasonable, as it is generally unlikely that an entire peninsula would be in a state of subsidence unless large-scale underground engineering activities—such as mineral resource extraction—were present. Furthermore, the Qisha Peninsula, another peninsula in Gangkou District, exhibited almost no subsidence points, which is also inconsistent with the dense-point advantage of SBAS-InSAR. Although that study failed to identify subsidence funnel signals in the reclamation zones of Gangkou District, it confirmed the fact that land subsidence exists in Gangkou District. In 2024 and 2026, Ming et al. and Gao et al. conducted time-series ground deformation monitoring in the Maowei Sea area of the Beibu Gulf [34,35]. The Maowei Sea is adjacent to the experimental area of this study, but the two areas do not overlap. Although the ground subsidence monitoring results from these two studies in the Maowei Sea area cannot be directly compared with those of this study, these two papers provide a detailed analysis of the relationships between various influencing factors—including precipitation, groundwater, biological activities, hydrological movements, and mangrove changes—and ground subsidence, offering valuable insights for this study in considering influencing factors beyond land reclamation.

(3) Implications. Compared with previously published studies, our research focuses specifically on the monitoring and assessment of land subsidence—a potential geohazard—in Gangkou District of Fangchenggang City. By integrating long-term time-series InSAR-derived subsidence results from radar remote sensing with long-term coastline change results from optical remote sensing, our study identified seven distinct subsidence funnel signals in Gangkou District, rather than wholesale subsidence of the entire Gangkou District or an absence of signals—a new finding not reported in previous literature. Additionally, we found that all seven subsidence funnels are located within reclaimed coastal zones, and that reclamation engineering activities are the dominant factor governing subsidence in this region, rather than merely one of multiple contributing factors without hierarchical distinction—another novel result not addressed in earlier studies. These findings provide a novel framework and valuable insights into the hidden hazards monitoring and assessment of other coastal reclamation cities.

4.5. Limitation and Future

(1) Limitations. The earliest large-scale land reclamation in Fangchenggang can be traced back to the Shatangjiang reclamation project in 1931, which created approximately 2 km^2 of land area through reclamation. Large-scale sea reclamation for agricultural land took place primarily in the 1950s and 1960s, with the Rongshutou reclamation project alone adding about 13 km^2 of land area. However, the earliest optical remote sensing imagery available for this study is declassified imagery from 1964 captured by U.S. reconnaissance satellites, allowing us to extract only the changes in land area from reclamation activities between 1964 and the present. Moreover, the earliest SAR satellite is the Seasat satellite, launched only in 1978. Considering the heavy workload and time-consuming of time-series InSAR data processing, this study only uses 266 scenes of Sentinel-1A SAR satellite data to obtain land subsidence results for the study area from 2016 to 2025. Although the accuracy and reliability of time-series InSAR technology have been validated in multiple published studies, and this paper also cross-validates two time-series InSAR methods, namely SBAS-InSAR and PS-InSAR, validation against field measurement data such as GNSS and leveling surveys is still lacking. Although land subsidence in the study area is primarily caused by reclamation, land subsidence in a region is often the result of multiple interacting factors.

This paper analyzes reclamation, precipitation, and groundwater factors, but the analysis of driving factors is still not comprehensive or detailed enough.

(2) Future work. In the future, we will consider using historical SAR data such as ERS-1/2 and Envisat ASAR from 1991 to 2012, as well as commercial satellite data including Radarsat, TerraSAR-X, ALOS, and COSMO-SkyMed, to obtain longer time-series land subsidence results for the study area. Moreover, to further validate the land subsidence results presented in this paper, future work will consider incorporating validation using field measurement data including GNSS and leveling surveys. Additionally, future work will consider incorporating analyses of additional factors such as built-up area expansion, and sea level rise. Furthermore, in 2015, we utilized aerial photogrammetry to obtain a high-resolution Digital Surface Model (DSM) covering the entire Fangchenggang City. In the future, we plan to conduct UAV remote sensing monitoring over the land subsidence areas identified by time-series InSAR to acquire high-resolution DSM data. By performing differential processing on the high-resolution DSMs obtained from the 2015 aerial photogrammetry and future UAV remote sensing campaigns, we can derive high-resolution land surface deformation results. This will serve to supplement and validate the land subsidence results derived from time-series InSAR monitoring. Additionally, these high-precision datasets can be used to simulate and assess the potential hazards posed by sea-level rise in the study area.

5. Conclusions

This study takes the typical land reclamation city—Fangchenggang City, China—as the study area. A total of 266 Sentinel-1A SAR images from 2016 to 2025 were used to obtain time-series land subsidence monitoring results over the past decade using the SBAS-InSAR method. In addition, multi-source optical remote sensing images, including declassified reconnaissance satellite images (KH), Landsat-8, and Sentinel-2, were used to extract coastline changes in the study area from 1964 to 2025. Influencing factors analysis of the study area was then conducted by integrating precipitation data and groundwater data. The conclusions of this paper are as follows:

(1) Using SBAS-InSAR and PS-InSAR methods, time-series InSAR land subsidence monitoring was conducted in the study area from 2016 to 2025, and the two methods of results were cross-validated. The results show good consistency between the two monitoring outcomes, demonstrating that the use of time-series InSAR methods for monitoring land subsidence in this area is reliable.

(2) Seven distinct subsidence areas were identified based on the time-series InSAR land subsidence results. Spatially, the land subsidence exhibits significant heterogeneity in distribution, mainly concentrated in the reclaimed land areas of the Qisha Peninsula and the Yuwan Peninsula. In the early completed reclamation areas, the land subsidence rate is generally less than -10 mm/yr and tends to stabilize; however, the maximum subsidence rate during the period from 2016 to 2025 reached as high as -163.53 ± 4.90 mm/yr. Temporally, the land subsidence rate in the study area shows a gradually decelerating trend over time, that is, the subsidence rate is relatively high in the early stage of reclamation and then gradually slows down, exhibiting an evolutionary characteristic of rapid initial subsidence followed by a slower rate.

(3) The coastline changes in the study area from 1964 to 2025 exhibit a three-stage temporal characteristic. Specifically, the land area increased by 2.23 ± 4.51 km^2, 14.28 ± 6.19 km^2, and 23.31 ± 4.51 km^2 during the periods 1964–1995, 1995–2008, and 2008–2025, respectively, with corresponding growth rate coefficients of 0.06, 0.78, and 1.01. The time-series InSAR land subsidence monitoring period of 2016–2025 in this study falls exactly within the third stage of rapid coastline change. The time-series InSAR subsi-

dence monitoring results and the coastline change results mutually validate each other, further demonstrating that the primary factor causing land subsidence in the study area is land reclamation.

(4) In addition to analyzing the impact of land reclamation, the study also examined influencing factors such as precipitation and groundwater. A comparison between the time-series InSAR land subsidence results and precipitation data revealed subtle fluctuating signals within the time-series subsidence data. These minor fluctuations mainly occurred during the peak precipitation months of February, June, August, and October. Specifically, when precipitation increased, land subsidence values in the study area exhibited a rebound phenomenon; conversely, when precipitation decreased, subsidence values declined normally. Furthermore, groundwater showed a positive correlation with the time-series InSAR land subsidence results.

Author Contributions: Conceptualization, Y.S. and K.Y.; methodology, Y.S. and K.Y.; software, K.Y. and M.Z. (Mingsheng Zhang); validation, J.T. and M.Z. (Mingsheng Zhang); formal analysis, K.Y. and M.Z. (Miaomiao Zhang); investigation, J.T.; resources, K.Y.; data curation, K.Y. and M.Z. (Mingsheng Zhang); writing—original draft preparation, Y.S.; writing—review and editing, Y.S. and K.Y.; visualization, K.Y. and M.Z. (Mingsheng Zhang); supervision, M.Z. (Miaomiao Zhang); project administration, M.Z. (Mingsheng Zhang); funding acquisition, Y.S. All authors have read and agreed to the published version of the manuscript.

Funding: This work was supported in part by the 2025 Henan Provincial Science and Technology Research and Development Plan Joint Fund (Discipline Category) Project under Grant 252103810060 and 252103810058, the Henan Provincial University Research Project in Humanities and Social Sciences under Grant 2021-ZDJH-047, and the Research Funds for the Henan University of Urban Construction under Grant 990/R-X2020014 and 990/K-H2023099.

Data Availability Statement: The Sentinel series data presented in this study are openly available in the Copernicus Data Space Ecosystem at https://dataspace.copernicus.eu/(accessed on 2 January 2026). The KeyHole (KH) and Landsat 8 optical remote sensing data are openly available in the United States Geological Survey (USGS) at https://earthexplorer.usgs.gov/ (accessed on 8 January 2024). The ASTER GDEM data presented in this study are openly available in the National Aeronautics and Space Administration (NASA) at https://asterweb.jpl.nasa.gov/gdem.asp (accessed on 9 May 2023). The GACOS atmosphere model data presented in this study are openly available in the Chang'an University at http://www.gacos.net/ (accessed on 4 January 2026). The Hydrological data presented in this study are openly available in the Department of Water Resources of Guangxi and the Statistics Bureau of Guangxi at http://slt.gxzf.gov.cn/ (accessed on 11 February 2026) and http://tjj.gxzf.gov.cn/ (accessed on 11 February 2026).

Acknowledgments: The authors would like to thank the European Space Agency (ESA) for providing the Sentinel series data and the United States Geological Survey (USGS) for providing the KeyHole (KH) and Landsat 8 optical remote sensing data. We would also like to thank the anonymous reviewers for their valuable comments and suggestions.

Conflicts of Interest: The authors declare no conflicts of interest.

References

1. Sun, Q.S.; Jiang, L.M.; Jiang, M.; Lin, H.; Ma, P.F.; Wang, H.S. Monitoring coastal reclamation subsidence in Hong Kong with distributed scatterer interferometry. *Remote Sens.* **2018**, *10*, 1738. [CrossRef]
2. Jiang, L.M.; Lin, H. Integrated analysis of SAR interferometric and geological data for investigating long-term reclamation settlement of Chek Lap Kok Airport, Hong Kong. *Eng. Geol.* **2010**, *110*, 77–92. [CrossRef]
3. Jiang, L.M.; Lin, H.; Cheng, S.L. Monitoring and assessing reclamation settlement in coastal areas with advanced InSAR techniques: Macao city (China) case study. *Int. J. Remote Sens.* **2011**, *32*, 3565–3588. [CrossRef]
4. Gong, Z.H.; Shi, L.Q.; Zhang, D.H.; Zhang, H.G. Comparative study on remote sensing of coastlines and reclamation of typical bays in China and Vietnam: Taking Fangcheng Bay and Haiphong Port as examples. *J. Mar. Sci.* **2022**, *40*, 62–72.

5. Hu, Y.; Barberopoulou, A.; Koch, M. Tracing the 2018 Sulawesi Earthquake and Tsunami's Impact on Palu, Indonesia: A Remote Sensing Analysis. *J. Mar. Sci. Eng.* **2025**, *13*, 178. [CrossRef]
6. Nicholls, R.J.; Lincke, D.; Hinkel, J.; Brown, S.; Vafeidis, A.T.; Meyssignac, B.; Hanson, S.E.; Merkens, J.-L.; Fang, J. A global analysis of subsidence, relative sea-level change and coastal flood exposure. *Nat. Clim. Change* **2021**, *11*, 338–342. [CrossRef]
7. Fang, J.; Nicholls, R.J.; Brown, S.; Lincke, D.; Hinkel, J.; Vafeidis, A.T.; Du, S.; Zhao, Q.; Liu, M.; Shi, P. Benefits of subsidence control for coastal flooding in China. *Nat. Commun.* **2022**, *13*, 6946. [CrossRef] [PubMed]
8. Santos, A.; Mileu, N. Coastal protection for tsunamis. *J. Mar. Sci. Eng.* **2024**, *12*, 2349. [CrossRef]
9. Batmanathan, N.M.; Pereira, J.J.; Shah, A.A.; Muhamad, N.; Sian, L.C. Land subsidence and coastal flood impact scenarios based on remote sensing in Selangor, Malaysia. *J. Mar. Sci. Eng.* **2025**, *13*, 1539. [CrossRef]
10. Sun, Y.F.; Jiang, L.M.; Liu, L.; Sun, Q.S.; Wang, H.S.; Hsu, H. Mapping Glacier Elevations and Their Changes in the Western Qilian Mountains, Northern Tibetan Plateau, by Bistatic InSAR. *IEEE J. Sel. Top. Appl. Earth Obs. Remote Sens.* **2018**, *11*, 68–78. [CrossRef]
11. Sun, Y.F.; Jiang, L.M.; Gao, N.; Gao, S.F.; Li, J.J. Estimation and Analysis of Glacier Mass Balance in the Southeastern Tibetan Plateau Using TanDEM-X Bi-Static InSAR during 2000–2014. *Atmosphere* **2024**, *15*, 364. [CrossRef]
12. Bai, L.; Li, Z.H.; Bürgmann, R.; Zhao, Y.; Jiang, L.M.; Cao, G.L.; Zhao, C.Y.; Zhang, Q.; Peng, J.B. Contributions of Climate Variability and Anthropogenic Activities to Confined Groundwater Storage in Hengshui, North China Plain. *Remote Sens.* **2023**, *15*, 4827. [CrossRef]
13. An, Y.; Shen, Q.; Shum, C.K.; Gao, F.; Zhang, X.; Jiang, L.M.; Wang, H. TS-InSAR assessment of groundwater overexploitation-land subsidence linkage: Hengshui case study. *J. Hydrol. Reg. Stud.* **2025**, *60*, 102489. [CrossRef]
14. Hu, B.; Li, W.; Lu, W.F.; Zhao, F.L.; Li, Y.B.; Li, R.J. Integrating InSAR Data and LE-Transformer for Foundation Pit Deformation Prediction. *Remote Sens.* **2025**, *17*, 1106. [CrossRef]
15. Ao, Z.R.; Hu, X.M.; Tao, S.L.; Hu, X.; Wang, G.Q.; Li, J.M.; Wang, F.; Hu, L.T.; Liang, X.Y.; Xiao, J.F.; et al. A national-scale assessment of land subsidence in China's major cities. *Science* **2024**, *384*, 301–306. [CrossRef] [PubMed]
16. Li, G.R.; Zhao, C.Y.; Wang, B.H.; Liu, X.J.; Chen, H.Y. Land Subsidence Monitoring and Dynamic Prediction of Reclaimed Islands with Multi-Temporal InSAR Techniques in Xiamen and Zhangzhou Cities, China. *Remote Sens.* **2022**, *14*, 2930. [CrossRef]
17. Huang, J.H.; Wang, B.H.; Cai, X.H.; Yan, B.J.; Li, G.R.; Li, W.H.; Zhao, C.Y.; Yang, L.Y.; Zheng, S.Z.; Cui, L.J. Coastal Reclamation Embankment Deformation: Dynamic Monitoring and Future Trend Prediction Using Multi-Temporal InSAR Technology in Funing Bay, China. *Remote Sens.* **2024**, *16*, 4320. [CrossRef]
18. Jiang, Z.; Shi, G.Q.; Wu, S.B.; Ding, X.L.; Zhao, C.Y.; Wong, M.S.; Lu, Z. Unveiling multimodal consolidation process of the newly reclaimed HKIA 3rd runway from satellite SAR interferometry, ICA analytics and Terzaghi consolidation theory. *Remote Sens. Environ.* **2025**, *318*, 114561. [CrossRef]
19. Zhang, Y.; Liu, S.Y.; Lan, K.; Wu, L.H.; Han, Y.K.; Liu, Y.; Yu, B.X. Land subsidence in urban lake-infilled areas detected by Radarsat-2 InSAR time-series: The case of Shahu and Nanhu Lake in Wuhan, China. *J. Hydrol.* **2026**, *672*, 135408. [CrossRef]
20. Abidin, H.Z.; Andreas, H.; Gumilar, I.; Fukuda, Y.; Pohan, Y.E.; Deguchi, T. Land subsidence of Jakarta (Indonesia) and its relation with urban development. *Nat. Hazards* **2011**, *59*, 1753–1771. [CrossRef]
21. Abidin, H.Z.; Andreas, H.; Gumilar, I.; Sidiq, T.P.; Fukuda, Y. Land subsidence in coastal city of Semarang (Indonesia): Characteristics, impacts and causes. *Geomat. Nat. Hazards Risk* **2013**, *4*, 226–240. [CrossRef]
22. Tosi, L.; Da Lio, C.; Teatini, P.; Strozzi, T. Land subsidence in coastal environments: Knowledge advance in the Venice coastland by TerraSAR-X PSI. *Remote Sens.* **2018**, *10*, 1191. [CrossRef]
23. Verberne, M.; Koster, K.; Lourens, A.; Gunnink, J.; Candela, T.; Fokker, P.A. Disentangling shallow subsidence sources by data assimilation in a reclaimed urbanized coastal plain, South Flevoland polder, the Netherlands. *J. Geophys. Res. Earth Surf.* **2023**, *128*, e2022JF007031. [CrossRef]
24. Park, S.; Kim, D.-J.; Lee, S.; Song, J.; Kim, J. Analysis of land subsidence characteristics according to reclamation and construction periods using Sentinel-1 time-series interferometry: A case study on the west coast of South Korea. *IEEE J. Sel. Top. Appl. Earth Obs. Remote Sens.* **2026**, *19*, 22315–22326. [CrossRef]
25. Lomibao, A.L.; Leal, G.A.; Mabaquiao, L.C.; Reyes, R.B. Ground deformation monitoring of reclaimed lands along Manila Bay Freeport Zone using PS-InSAR technique. *Int. Arch. Photogramm. Remote Sens. Spat. Inf. Sci.* **2024**, *XLVIII-4/W8-2023*, 335–342. [CrossRef]
26. Yuan, Y.; Wang, L. Assessment of land subsidence and future flood hazards for coastal cities of the Gulf of Mexico using time series InSAR. *Nat. Hazards* **2026**, *122*, 446. [CrossRef] [PubMed]
27. Catalão, J.; Raju, D.; Nico, G. InSAR maps of land subsidence and sea level scenarios to quantify the flood inundation risk in coastal cities: The case of Singapore. *Remote Sens.* **2020**, *12*, 296. [CrossRef]
28. Fattahi, H.; Amelung, F. DEM error correction in InSAR time series. *IEEE Trans. Geosci. Remote Sens.* **2013**, *51*, 4249–4259. [CrossRef]
29. Xiao, R.; Yu, C.; Li, Z.; He, X. Statistical assessment metrics for InSAR atmospheric correction: Applications to generic atmospheric correction online service for InSAR (GACOS) in eastern China. *Int. J. Appl. Earth Obs. Geoinf.* **2021**, *96*, 102289. [CrossRef]

30. Ma, Z.; Liu, J.; Liu, X.; Zhou, C.; Hu, J.; Cui, Y.; Qin, S.; Huang, T.; Li, Z. Go extra miles: An additional error correction procedure aimed to further improve phase unwrapping accuracy and reduce creep model uncertainty. *J. Geophys. Res. Solid Earth* **2022**, *127*, e2021JB022478. [CrossRef]
31. Olsen, K.M.; Calef, M.T.; Agram, P.S. Contextual uncertainty assessments for InSAR-based deformation retrieval using an ensemble approach. *Remote Sens. Environ.* **2023**, *287*, 113456. [CrossRef]
32. Luo, T.Y.; Gao, E.T.; Zhao, W.; Xiao, Y.Z.; Li, S.X. Deformation detection and cause analysis of Beibu gulf based on PS-InSAR in Guangxi. *Hydrogr. Surv. Charting* **2024**, *44*, 31–35.
33. Ming, X.Y.; Tian, Y.C.; Zhang, Q.; Tao, J.; Zhang, Y.L.; Lin, J.L. Monitoring and analyzing land subsidence in Qinfang, Guangxi based on Sentinel-1A data. *Remote Sens. Nat. Resour.* **2024**, *36*, 35–48. [CrossRef]
34. Ming, X.Y.; Tian, Y.C.; Zhang, Q.; Tao, J.; Zhang, Y.L.; Lin, J.L. Monitoring and analysis of surface deformation of Tidal Flat in Maowei Sea on the basis of Sentinel active and passive remote sensing. *Natl. Remote Sens. Bull.* **2024**, *28*, 2306–2319. [CrossRef]
35. Gao, E.T.; Liu, J.; Li, S.J.; Zhou, G.Q.; Fu, B.L.; Li, S.X. Multi-dimensional spatiotemporal monitoring and analysis of tidal flats in the Maowei Sea using integrated optical remote sensing and SAR. *Acta Geod. Cartogr. Sin.* **2026**, *55*, 632–646. [CrossRef]
36. Zhou, X.J.; Li, X.M.; Ma, Y.; Wu, P.Q. Analysis of shoreline changes in the Fangcheng Bay of Guangxi based on remote sensing technique. *J. Mar. Sci.* **2014**, *32*, 47–55. [CrossRef]
37. Meng, X.W.; Zhang, C.Z. *Overview of Marine Environment and Resources in Guangxi*; China Ocean Press: Beijing, China, 2014.
38. Su, H.Y.; Li, J.M. Land Reclamation Management according to Ecosystem-based Comprehensive Cost-benefit Analysis. *J. Ocean Univ. China* **2020**, *1*, 75–83. [CrossRef]
39. Torres, R.; Snoeij, P.; Geudtner, D.; Bibby, D.; Davidson, M.; Attema, E.; Potin, P.; Rommen, B.; Floury, N.; Brown, M.; et al. GMES Sentinel-1 mission. *Remote Sens. Environ.* **2012**, *120*, 9–24. [CrossRef]
40. Richelson, J. The keyhole satellite program. *J. Strateg. Stud.* **1984**, *7*, 121–153. [CrossRef]
41. Chen, C.; Fu, J.Q.; Zhang, S.; Zhao, X. Coastline information extraction based on the tasseled cap transformation of Landsat-8 OLI images. *Estuar. Coast. Shelf Sci.* **2019**, *217*, 281–291. [CrossRef]
42. Ding, Y.X.; Yang, X.M.; Jin, H.L.; Wang, Z.H.; Liu, Y.M.; Liu, B.; Zhang, J.Y.; Liu, X.L.; Gao, K.; Meng, D. Monitoring coastline changes of the Malay Islands based on Google Earth Engine and dense time-series remote sensing images. *Remote Sens.* **2021**, *13*, 3842. [CrossRef]
43. Pardo-Pascual, J.E.; Almonacid-Caballer, J.; Cabezas-Rabadán, C.; Fernández-Sarria, A.; Armaroli, C.; Ciavola, P.; Montes, J.; Souto-Ceccon, P.E.; Palomar-Vázquez, J. Assessment of satellite-derived shorelines automatically extracted from Sentinel-2 imagery using SAET. *Coast. Eng.* **2024**, *188*, 104426. [CrossRef]
44. Liu, G.L.; Li, J.Y.; Nie, P. Tracking the history of urban expansion in Guangzhou (China) during 1665–2017: Evidence from historical maps and remote sensing images. *Land Use Policy* **2022**, *112*, 105773. [CrossRef]
45. Hou, Z.; Liu, Y.; Zhang, L.; Ai, H.; Sun, Y.; Han, X.; Zhu, C. 2OC: A general automated orientation and orthorectification method for Corona KH-4B panoramic imagery. *Remote Sens.* **2023**, *15*, 5116. [CrossRef]
46. Ghuffar, S.; Bolch, T.; Rupnik, E.; Bhattacharya, A. A pipeline for automated processing of declassified Corona KH-4 (1962–1972) stereo imagery. *IEEE Trans. Geosci. Remote Sens.* **2022**, *60*, 5629614. [CrossRef]
47. Jacobsen, K. Calibration and validation of CORONA KH-4B to generate height models and orthoimages. *ISPRS Ann. Photogramm. Remote Sens. Spat. Inf. Sci.* **2020**, *V-1-2020*, 151–155. [CrossRef]
48. Han, H.J.; Zeng, Q.M.; Jiao, J. Quality assessment of TanDEM-X DEMs, SRTM and ASTER GDEM on selected Chinese sites. *Remote Sens.* **2021**, *13*, 1304. [CrossRef]
49. Zhang, X.S.; Li, Z.H.; Liu, Z.J. Reduction of atmospheric effects on InSAR observations through incorporation of GACOS and PCA into small baseline subset InSAR. *IEEE Trans. Geosci. Remote Sens.* **2023**, *61*, 5209115. [CrossRef]
50. Berardino, P.; Fornaro, G.; Lanari, R.; Sansoti, E. A new algorithm for surface deformation monitoring based on small baseline differential SAR interferogram. *IEEE Trans. Geosci. Remote Sens.* **2002**, *40*, 2375–2383. [CrossRef]
51. Ferretti, A.; Prati, C.; Rocca, F. Nonlinear subsidence rate estimation using permanent scatterers in differential SAR interferometry. *IEEE Trans. Geosci. Remote Sens.* **2000**, *38*, 2202–2212. [CrossRef]
52. Bishop-Taylor, R.; Nanson, R.; Sagar, S.; Lymburner, L. Mapping Australia's dynamic coastline at mean sea level using three decades of Landsat imagery. *Remote Sens. Environ.* **2021**, *267*, 112734. [CrossRef]
53. Doherty, Y.; Harley, M.D.; Vos, K.; Splinter, K.D. A Python toolkit to monitor sandy shoreline change using high-resolution PlanetScope cubesats. *Environ. Model. Softw.* **2022**, *157*, 105512. [CrossRef]
54. Wu, T.; Liu, P.; Yu, J.; Wen, T. Comparative study on different tide level correction methods in remote sensing extraction of coastline under balanced profile model. *J. Trop. Oceanogr.* **2023**, *42*, 52–62. [CrossRef] [PubMed]
55. Caldareri, F.; Sulli, A.; Parrino, N.; Dardanelli, G.; Todaro, S.; Maltese, A. On the shoreline monitoring via earth observation: An isoradiometric method. *Remote Sens. Environ.* **2024**, *311*, 114286. [CrossRef]
56. Himmelstoss, E.A.; Henderson, R.E.; Kratzmann, M.G.; Farris, A.S. *Digital Shoreline Analysis System (DSAS) Version 5.1 User Guide*; U.S. Geological Survey Open-File Report 2021–1091; U.S. Geological Survey: Reston, VA, USA, 2021. [CrossRef]

57. Gao, E.T.; Li, S.X.; Li, S.J.; Ma, X.S.; Xiao, Y.Z. Analysis of Guangxi coastline changes from 1987 to 2021 based on multi-source remote sensing. *Hydrogr. Surv. Charting* **2024**, *44*, 68–72.
58. *DD 2014-11*; Technical Code for Interferometric Radar Data Processing of Land Subsidence. China Geological Survey: Beijing, China, 2014.
59. Sun, H.; Peng, H.; Zeng, M.; Wang, S.; Pan, Y.; Pi, P.; Xue, Z.; Zhao, X.; Zhang, A.; Liu, F. Land subsidence in a coastal city based on SBAS-InSAR monitoring: A case study of Zhuhai, China. *Remote Sens.* **2023**, *15*, 2424. [CrossRef]

Disclaimer/Publisher's Note: The statements, opinions and data contained in all publications are solely those of the individual author(s) and contributor(s) and not of MDPI and/or the editor(s). MDPI and/or the editor(s) disclaim responsibility for any injury to people or property resulting from any ideas, methods, instructions or products referred to in the content.